Liquid migration in flowing granular media

Thijmen Hagen

December 23, 2020

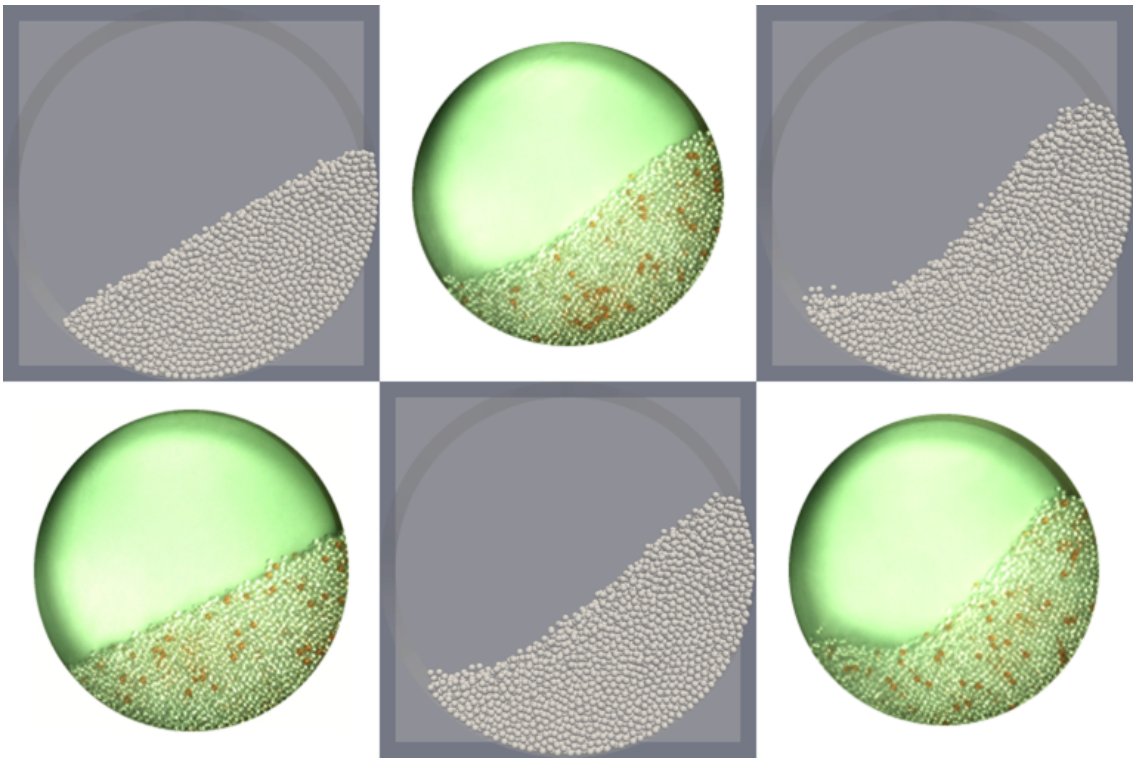

Committee

Chairman: Prof. Dr. Stefan Luding

Supervisor: Dr. Ahmed Jarray

Member: Prof. Dr. Devaraj van der Meer

Abstract

Liquid induced cohesion has a significant effect on the flow characteristics of wet granular assemblies. In this work, discrete element method (DEM) simulations are compared with experiments of granular flow behavior in a rotating drum. Without calibration, the simulations match the experiments for intermediate rotation speed in the dry case. When liquid is added, the angle of repose of the simulations is lower than that of the experiments. The flow speed and granular temperature show good qualitative agreement. For a small capillary force, the liquid migrates to the center of the particle bed in the drum, while for a high capillary force, the liquid migrate away from this center. In both cases, this is caused by the liquid migrating away from regions of high strain rate.

Contents

1 Introduction

Wet granular flows occur everywhere in nature, e.g. mud flow, landslides and avalanches, [1]. They also have direct application in numerous industrial processes. For instance, the mixing of wet granular materials is important in the pharmaceutical [2, 3] and food industries [4, 5]. For these processes it is important to understand the interaction between liquid and granular particles. The interstitial liquid forms capillary bridges between neighboring particles [6], influencing the flow [7, 8, 9]. The distribution of liquid is in turn influenced by the flow of particles.

A simple and practical geometry to study the flow of granular materials is the rotating drum. Since this apparatus produces repeating avalanches or a continuous granular flow, it has been used extensively to study the behaviour of dry particles in both experiments and simulations [10, 11]. The flow of granular material with added liquid has also been investigated in the rotating drum [12, 13, 14] using both experiments and simulations.

This interplay between liquid and particles has also been studied in a split bottom shear cell [15, 16], where the particles are sheared. The mixing of wet granular material has also been investigated by Schmelzle and Nirschl [17]. The current models for liquid migration are build on a large number of approximations and are not yet fully tested [18, 19, 20], and the currently widely used ones assume that liquid is distributed equally between the two particles when a capillary bridge ruptures.

The DEM code MercuryDPM [21] is able to simulate wet granular material and has been tested on the split bottom shear cell [22]. In this work, the experiments performed by Jarray et al. [12] are reproduced using MercuryDPM. In these experiments, a rotating drum has been used at varying rotation speeds, partially filled with wet granular particles. The capillary force of the liquid has been varied.

2 Methods

2.1 DEM simulations

Simulations have been performed with the MercuryDPM code [21], `www.mercurydpm.org`, developed in the MSM research group at the university of Twente. MercuryDPM is a code based on the discrete particle method (DEM) [23], which means that each of the particles inside the drum is simulated individually. For each particle, the velocity and position are updated at every time step using the forces acting on the particles. In these simulations, the particles experience a force of gravity, contact forces between particles, contact forces between a particle and the wall and adhesive forces due to the liquid. The force due to gravity f_g is given by

$$f_g = m_p \cdot g, \tag{1}$$

where m_p is the particle mass and $g = 9.81$ m/s^2 the gravitational acceleration. The contact force is given by a linear spring dashpot model [24], which means that the normal forces f^n between particles or between particle and wall are given by

$$f^n = k\delta + \gamma_0 v_n, \tag{2}$$

where k is the spring stiffness, δ the overlap between the particles, γ_0 the viscous damping coefficient and v_n the relative normal velocity between the two particles. This assumes that the particles are rigid, perfect spheres that do not deform on contact.

2.2 Liquid models

The models for liquid migration and capillary forces are based on models provide by Willet et al. [25]. These models were implemented in MercuryDPM and tested using a split bottom shear cell by Roy et al. [26]. In this thesis, these models are tested using a rotating drum apparatus.

The liquid bridge model does not explicitly simulate the liquid, but considers the forces exerted by the liquid on the particles. To achieve this, the liquid is initially added as liquid films on the particles, by storing the volume of a liquid film as a property of that particle. When two particles come into contact, ($\delta \geq 0$), a capillary bridge is formed between them and the stored liquid is moved to the new capillary bridge. The maximum volume V_{max} of the capillary bridges is

$$V_{max} = \beta r_p^3, \tag{3}$$

where β is the maximum bridge volume coefficient, which is a parameter of the liquid migration model. If the total available liquid is less than V_{max}, then all liquid is moved to the capillary bridge. If the total available liquid is more than V_{max}, then liquid is moved from each particle in proportion to the liquid film volume of each particle. The excess liquid remains in the liquid film to ensure conservation of liquid volume.

After a capillary bridge is formed, it exerts an adhesive force on the particles it connects. This capillary force is given by

$$f_c^{ij} = \frac{f_c^{max}}{1 + 1.05\bar{S} + 2.5\bar{S}^2}, \tag{4}$$

where

$$\bar{S} = S\sqrt{r_p/V_b} \tag{5}$$

is the separation distance S normalized by the square root of the particle radius divided by the bridge volume. The maximum capillary force, which occurs when the particles are in contact with each other, $S = 0$, is given by

$$f_c^{max} = 2\pi r_p \sigma \cos\theta, \tag{6}$$

where σ is the surface tension of the liquid and θ the contact angle. When the two particles connected by a capillary bridge move farther away from each other than the critical separation distance

$$S_c = \left(1 + \frac{\theta}{2}\right) V_b^{1/3} \tag{7}$$

the bridge ruptures. This means that there is no longer a capillary force between the two particles, and the liquid that was in the capillary bridge is distributed between the two particles. The liquid is divided equally between the two particle. This liquid is then immediately distributed amongst the liquid film of the particle and the other existing capillary bridges connected to this particle. A fraction C_D of this half of the bridge volume is distributed evenly between the existing bridges.

The remaining fraction $1-C_D$ is stored in the particle's liquid film as shown schematically in Figure 1. $C_D = 1$ means that most particles will have no available liquid in their liquid film, and existing bridges will grow much faster than for lower values of C_D.

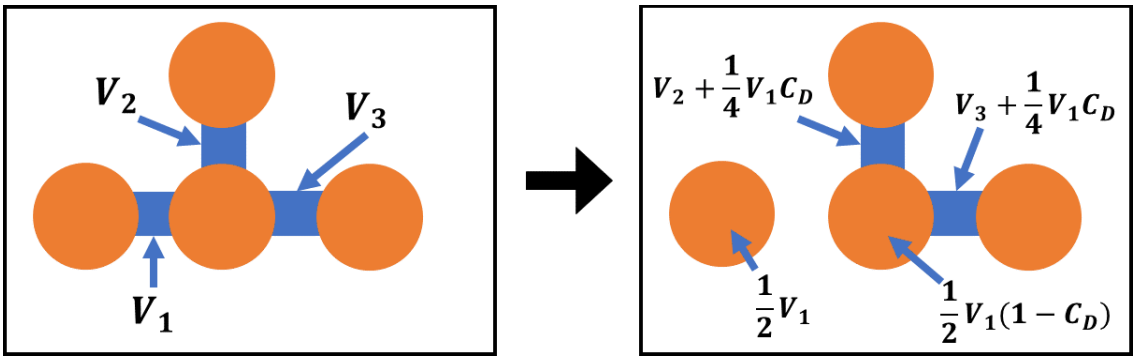

Figure 1: Schematic explanation of the bridge rupture code adapted from Mani et al [16] and Roy et al [26].

A theoretical maximum value of $\beta = 0.058$ was determined by Roy et al [26, 27], to ensure the pendular state, see Figure 4a. This value is based on the situation shown in Figure 2, where three particles are in contact with each other an connected by three capillary bridges. For $\beta > 0.058$, these bridges will coalesce, which means that the system is no longer in the pendular state, but has transitioned into the funicular state, see Figure 4b. However, Roy et al's simulations were performed with a much smaller amount of liquid present than were used in this thesis.

In this thesis, each interaction is approximated as a pendular capillary bridge. This means that only bridges are formed between two particles, but the theoretical maximum bridge volume can be exceeded. In order to find reasonable liquid migration model values, β was varied in the range $0.03 - 2$.

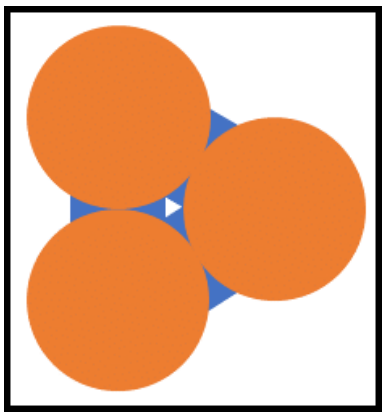

Figure 2: Schematic representation for the reasoning behind the maximum value of $\beta = 0.058$, as set by Roy et al [26, 27]. When three particles are in contact with each other and connected by capillary bridges, the bridges will coalesce for $\beta > 0.058$, trasitioning from the pendular to the funicular state.

2.3 Alteration to MercuryDPM

An inconsistency was found in the code of MercuryDPM. In the situation shown in Figure 3, where two particle make contact, but have no available liquid in the liquid films, no bridge can be formed. When a liquid bridge ruptures, a part of this liquid is distributed amongst the existing bridges. But, the contact where no bridge was formed is not considered an existing bridge, and thus no liquid is transferred. It is more physically correct for the liquid to form a new bridge at this contact as soon as liquid is available. This has been altered in MercuryDPM in this work.

The impact of alteration to MercuryDPM to the simulations was tested by first using the original code. The alteration to the code was only added after the first simulations were finished, it will be noted in this paper where the alteration is made.

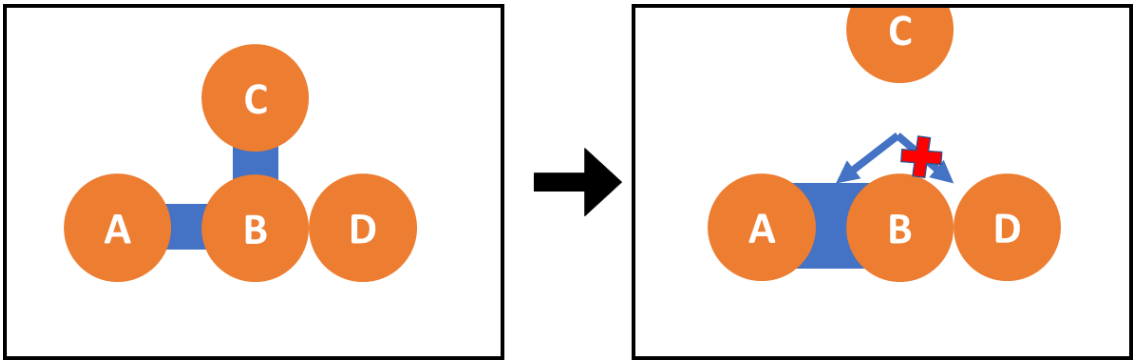

Figure 3: Schematic explanation of the situation in which the rupture code does not behave as expected. When particles B and D came into contact, both liquid films were empty, so no liquid bridge is formed. When a different capillary bridge connected to B ruptures, some of this liquid is redistributed among the existing bridges connected to B. But since there is no bridge between B and D, this contact is not considered. In the altered rupture code, some of the liquid will be used to form a new bridge between particle B and D.

2.4 Experimental setup

In order to have a way of validating the simulations, the parameters were closely matched to the experiments performed by A. Jarray [12]. The setup consists of a rotating drum, made of a cylinder of poplar wood, with an inner diameter D of 121 mm and a width L of 22 mm. This cylinder is held between two circular Plexiglas plates (PMMA) of 5 mm thickness to allow optical access. These were coated with Fluorinated Ethylene Propylene (FEP) to prevent wet glass particles sticking to the walls. The drum apparatus is rotated around it's axis at a variable speed. The drum is filled with monodisperse borosilicate glass particles. These particles have radius $r_p = 1.25$ mm and a density of $\rho_p = 2500$ kg/m^3. A total mass of

about $m_T = 0.125$ kg of particles was used to fill the drum to 35% of its volume. Images of the rotating drum were recorded using a MotionBLITZ EoSens high speed camera working at a speed of 460 fps.

In order to investigate the impact of capillary bridges on the flow properties, liquid was added to the drum. This liquid forms capillary bridges between the particles, resulting in adhesive forces. Depending on the amount of liquid, the system can be in three different states, see Figure 4. If the amount of liquid is small, only bridges between pairs of particles exist, which is called the pendular state. If more liquid is added, bridges will coalesce and form bridges between three or more particles, which is called the funicular state. If even more liquid is added, all the space between the particles is filled with liquid, this is called the capillary state. In the experiments, the system was kept in the pendular state by adding only 4 ml of liquid.

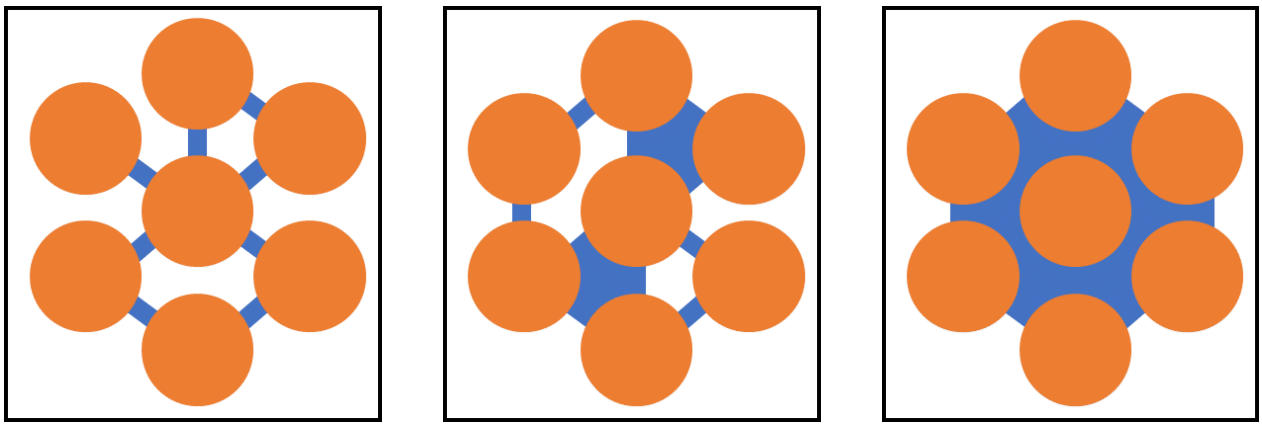

(a) *(b)* *(c)*

Figure 4: Three different states of liquid content:
In the pendular state, a, capillary bridges exist between pairs of particles.
In the funicular state, b, bridges exist between three or more particles at the same time.
In the capillary state, c, the liquid fully saturates the space between the particles.

The capillary force F_c of the liquid is given by

$$F_c = 2\pi\gamma r_p \cos\theta_c. \tag{8}$$

This was varied through the surface tension γ and contact angle θ_c. This was accomplished by using various fractions of ethanol and water, and by modifying the surface properties of the particles using a chemical silanization process.

The front and back wall of the drum were coated to prevent the particles sticking to these walls. In the simulation this is reproduced by not forming capillary bridges upon contact between a particle and these walls. The cylindrical wall is not coated in the experiments

allowing capillary bridges to form between particle and this wall. The wall does not have a liquid film, so when forming a bridge, all the liquid has to come from the particle. And when a bridge ruptures, all the liquid is returned to the particle, instead of the wall getting 50% of the liquid as well.

Table 1 summarizes the parameters used in experiment and simulation.

Paramater	Symbol	Value
Drum diameter	D	121 mm
Drum length	L	22 mm
Particle radius	r_p	1.25 mm
Particle density	ρ_p	2500 kg/m^3
Filling level	-	35%
Young's modulus	Y	$6.4 \cdot 10^{10}$ N/m^2
Poisson ratio	ν	0.2
Liquid content	V_{liq}	4 ml

Table 1: An overview of all the parameters used in the simulations.

2.5 Particle placement

The particles are initially placed on a square grid inside the drum, see Figure 5a. The particles are then allowed to fall down due to gravity and settle in a random packing, while the drum is not rotating. Because the particles are placed in a grid, there are no forces to move the particles in the axial direction, resulting in the particles staying in 2D planes until the drum starts rotating. To prevent this, one of the particles is places at an offset z-position (axial direction), which results in a more random packing at the beginning of the simulation. Figure 5b compares a simulation where this particle at offset z-position is used (right) with a simulation where this particle is not used (left). The left simulation clearly shows the particles staying in separate 2D planes.

In the experiments, a total mass of about $m_T = 0.125$ kg of particle was used, which corresponds to a filling level of 35%. The number of particles N_p can be calculated from the total mass, particle radius and particle density as

$$\begin{aligned} N_p &= m_T/m_p \\ &= m_T/\left(\rho_p \frac{4}{3}\pi r_p^3\right) \\ &\approx 6112. \end{aligned} \tag{9}$$

In order to confirm that the number of particles is correct, the filling level is tested in a simulation. Using the formula for the area of a circular segment [28], the height from the bottom of the drum that corresponds with a filling level of 35% is calculated. Figure 5c shows a red line at this height of the drum, when the particles are settled, before the drum starts rotating. It is shown that the particles fill approximately 35% of the drum, so $N_p = 6112$ particles will be used throughout this thesis.

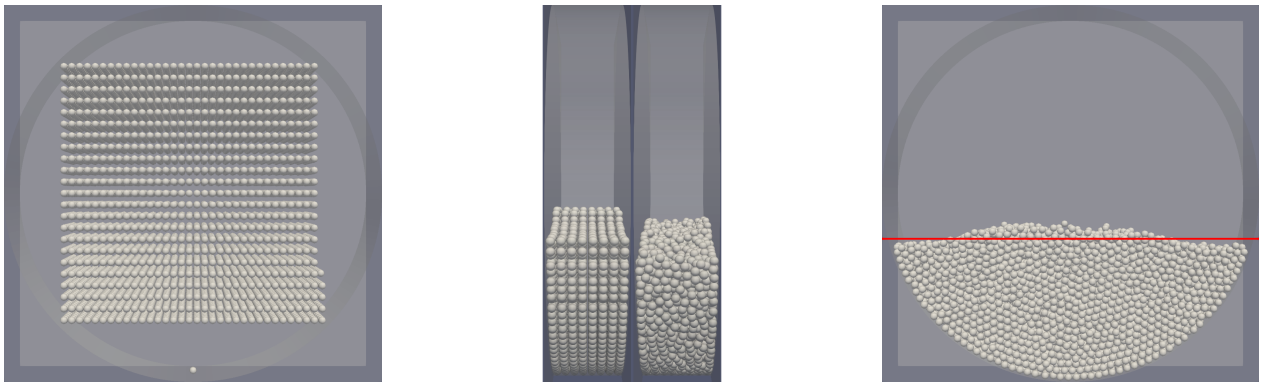

(a) *(b)* *(c)*

Figure 5: Three snapshots explaining the particle placement. (a) shows the initial placement of the particles in a square grid inside the drum. (b) shows a side view of the simulation just before the drum starts rotating. The left image shows a simulation that does not have a particle at offset z-direction, the right image shoes a simulation that does have this particle. (c) shows the simulation just before the drum starts rotating. The red line corresponds to 35% filling level, confirming that the particles fill about 35% of the drum.

After the particles have settled, the drum starts rotating. To ensure that the particles are well settled, the kinetic energy of the system is plotted as a function of time, see Figure 6. The blue, red and green lines corresponds to a simulation with rotation speed $\Omega = 5$, 25 and 45 RPM, respectively. Initially, when the particles are falling, the total kinetic energy of the system is on the order of 10^{-2} J. After 0.5 seconds, the particles have settled, and the total kinetic energy is on the order of 10^{-7} J. At $t = 0.5$ s, the drum starts rotating and the kinetic energy increases to the range of 10^{-5}-10^{-3} J, depending on the rotation speed of the drum. For the lowest rotation speed, which results in the lowest kinetic energy level, the kinetic energy is still two orders of magnitude lower before the drum starts rotating then after. This means that the particles have enough time to settle in 0.5 seconds.

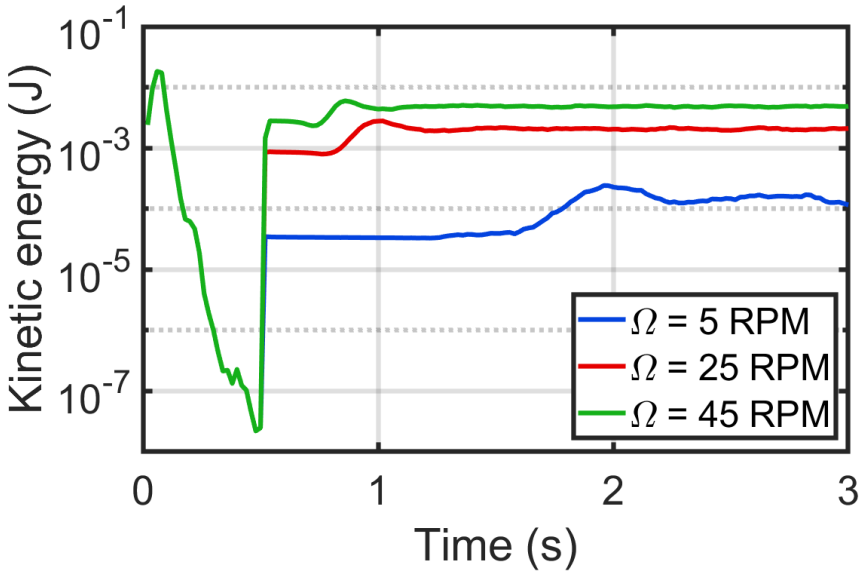

Figure 6: The kinetic energy of the particles as a function of time. The three curves correspond to different rotation speeds of the drum.

2.6 Time step

The collision times for a contact between two particles or between a particle and the wall are calculated from the elastic constant k_n and damping coefficient γ_n [29], which are calculated using hookes law [30]. For a collision between two particles $n = 1, 2$, with mass m_n, radius r_n, Poisson ratio ν_n, Young's modulus Y_n, relative velocity v and restitution coefficient e, the the collision time t_c is given by

$$
\begin{aligned}
\frac{1}{m^*} &= \frac{1}{m_1} + \frac{1}{m_2} \\
\frac{1}{r^*} &= \frac{1}{r_1} + \frac{1}{r_2} \\
\frac{1}{Y^*} &= \frac{(1-{\nu_1}^2)}{Y_1} + \frac{(1-{\nu_2}^2)}{Y_2} \\
k_n &= \frac{16}{15}\sqrt{r^*}Y^*\left(\frac{15m^*v^2}{16\sqrt{r^*}Y^*}\right)^{1/5} \\
\gamma_n &= \sqrt{\frac{4m^*k_n}{1+\left(\pi/\ln\left(e\right)\right)^2}} \\
\omega &= \sqrt{2k_n/m^* - \left(\gamma_n/m^*\right)^2} \\
t_c &= \pi/\omega
\end{aligned}
\tag{10}
$$

Since the relative velocity varies with each collision, a representative value has to be used. For this a value of $v = 1$ has been used. This value does not need to be exact, because $t_c \propto v^{-1/5}$, so variations in velocity have little impact on the collision time. Using these equations, the collision time between two particles is $t_{c_{pp}} = 8.4 \cdot 10^{-6}$ s, while for a particle-wall collision, it is $t_{c_{pw}} = 1.5 \cdot 10^{-5}$ s.

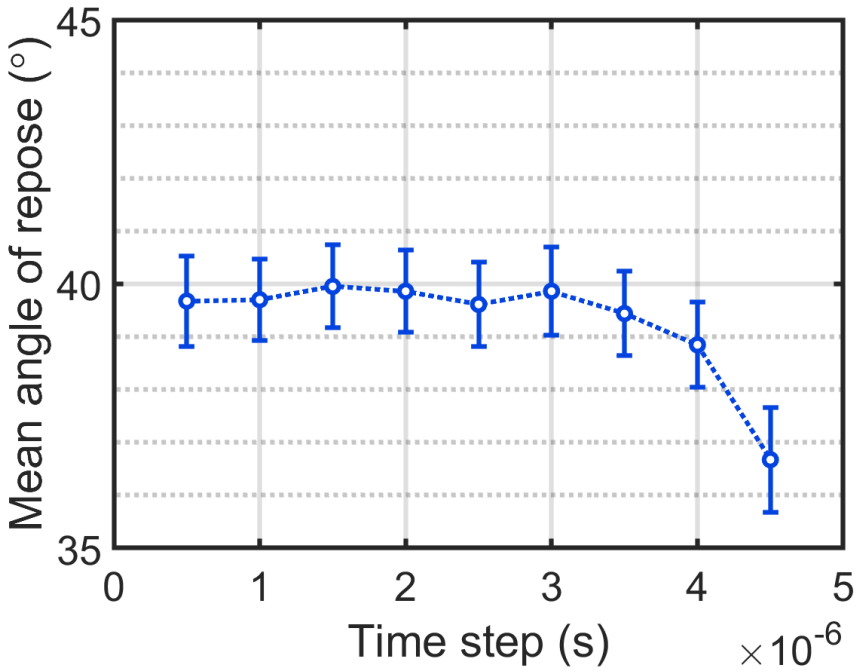

Figure 7: Mean angle of repose as a function of the time step for the dry case at $\Omega = 25$ RPM.

For the simulation to be stable, the time step should be smaller then the smallest collision time, $t_{c_{pp}} = 8.4 \cdot 10^{-6}$ s. Time steps in the range between $dt = 5 \cdot 10^{-7}$ s and $dt = 5 \cdot 10^{-6}$ s have been tested for the dry case at $\Omega = 25$ RPM. For the the simulation with $dt = 5 \cdot 10^{-6}$ s, the particles reach velocities of 10^3 m/s, which means that this simulation is unstable. For the simulations with the smaller time steps, the mean angle of repose is calculated. This is the angle of the surface of the bed, the method for calculating the angle of repose is explained in Section 2.7. Figure 7 shows the mean angle of repose as a function of time step. By decreasing the time step, the mean angle of repose converges, meaning that the system is not stable for the higher time steps. For time steps smaller than $dt = 3.5 \cdot 10^{-6}$ s, the mean angle of repose is converged enough to assume the system to be stable. From here on, a time step of $dt = 2.5 \cdot 10^{-6}$ s will be used.

2.7 Analysis methods

MercuryDPM [21] can return many properties of the particles and of the capillary bridges. In this work, we will extract the position, velocity and liquid content of each particle is used. The liquid content consists of the volume in the liquid film and half of the volume of all connected capillary bridges, ensuring that all liquid is counted once. From these properties of the particles, a number of properties were calculated using in-house Python codes and smoothed using point volume interpolation implemented in ParaView [31].

2.7.1 Angle of repose

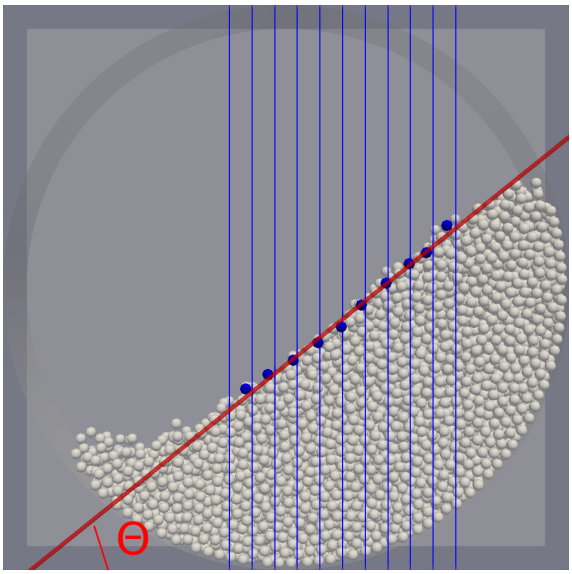

Figure 8: Visual explanation of the angle of repose calculation. The drum is divided into bins along the horizontal direction, in which the highest particle is taken. A linear fit is produced through these highest particles, representing the surface of the bed. The angle of repose is the angle between this surface and a horizontal line.

The angle of repose is the angle between the surface of the bed and a horizontal line. In order to find the surface of the bed, the drum is subdivided into bins, along the horizontal direction. For each bin, the highest particle is detected, and their coordinates are polyfitted using a linear function. Because the surface assumes an S-shape for higher rotation speeds, the surface of the bed is only calculated in the upper section of the surface. A representation of this method can be seen in Figure 8.

Since the particles are sometimes bouncing off the rest of the bed, this might disturb the calculation of the surface. The error due to this effect is expected to be insignificant, since the angle of the surface is calculated using 20 bins, meaning that one or a few particles have only a small impact on the angle calculation.

2.7.2 Flow speed

Another property that has been calculated to analyse the simulations is the flow speed. The flow speed is the velocity of the particle relative to the drum, and is a measure of mobility of the particles in an avalanche. The flow speed ϕ_i of particle i is calculated as

$$\phi_i = \sqrt{\left(v_{i,x} - v_{i,\omega x}\right)^2 + \left(v_{i,y} - v_{i,\omega y}\right)^2} \tag{11}$$

where $\overrightarrow{v_i} = (v_{i,x}, v_{i,y})$ is the velocity of particle i and $\overrightarrow{v_{i,\omega}} = (v_{i,\omega x}, v_{i,\omega y})$ is the drum wall velocity at the position of particle i. The flow speed is then smoothed and averaged over 30 time steps, corresponding to 0.3 s.

2.7.3 Granular temperature

The granular temperature is a measure for relative motion between particles. For regions where the particles move together like a solid, the granular temperature is small, while it is higher for regions where the particle are flowing and have many collisions with each other. The granular temperature T_i of particle i can be calculated from the flow speed as

$$T_i = \frac{1}{2}\left(\left(\phi_{i,x} - \phi_{av,x}\right)^2 + \left(\phi_{i,y} - \phi_{av,y}\right)^2\right) \tag{12}$$

where $\overrightarrow{\phi_{av}} = (\phi_{av,x}, \phi_{av,y})$ is the average flow speed of the particles within 3 particle radii from particle i. The granular temperature is then also smoothed. The granular temperature is calculated for a single time step, without taking the average over time steps.

2.7.4 Liquid distribution

To visualize the position of liquid in the particles bed, the amount of liquid on each particle is used. This value takes into account both the liquid in the liquid film and half of the liquid of the connected capillary bridges. This property is smoothed and averaged over 0.3 s.

2.7.5 Strain rate

Using Paraview, a approximation of the strain rate $\dot{\epsilon}_s$ can be calculated. For each particle, search area with radius $r_s = 3r_p$ is used. Between the particles inside this search radius, the two particles are found that have the largest difference in velocity. The absolute value of this difference is then taken and divided by twice the search radius to give an approximation of the strain rate.

$$\dot{\epsilon}_s = \frac{\max\left(|v_i - v_j|\right)}{2r_s} \tag{13}$$

This strain rate is then smoothed and averaged over 0.3 s.

A better method of calculating the strain rate was developed by Prof. dr. Stefan Luding. This method is used in Section B to verify the approximation using Paraview.

3 Results

3.1 Dry case

To confirm the accuracy of the simulations, the first simulations are performed without any liquid present, where the only forces acting on the particles are the contact forces and gravity. The rotation speed of these simulations are varied from 5 to 45 RPM, which corresponds to a variation in the Froude number from 0.04 to 0.37. The Froude number, $Fr = \sqrt{\frac{\omega^2 D}{2g}}$, represents the ratio of centrifugal to gravitational acceleration. Figure 9 shows snapshots of the experiments and simulations side by side for different rotation speeds. A good agreement between simulation and experiment can be seen. For low rotation speeds, at 5 RPM, the particles on the surface flow downwards in a slow manner, resulting in a flat surface of the bed. For high rotation speeds, at 45 RPM, the particles are moved upwards with more energy, and they consequently fall down with more energy, resulting in an S-shaped surface of the bed.

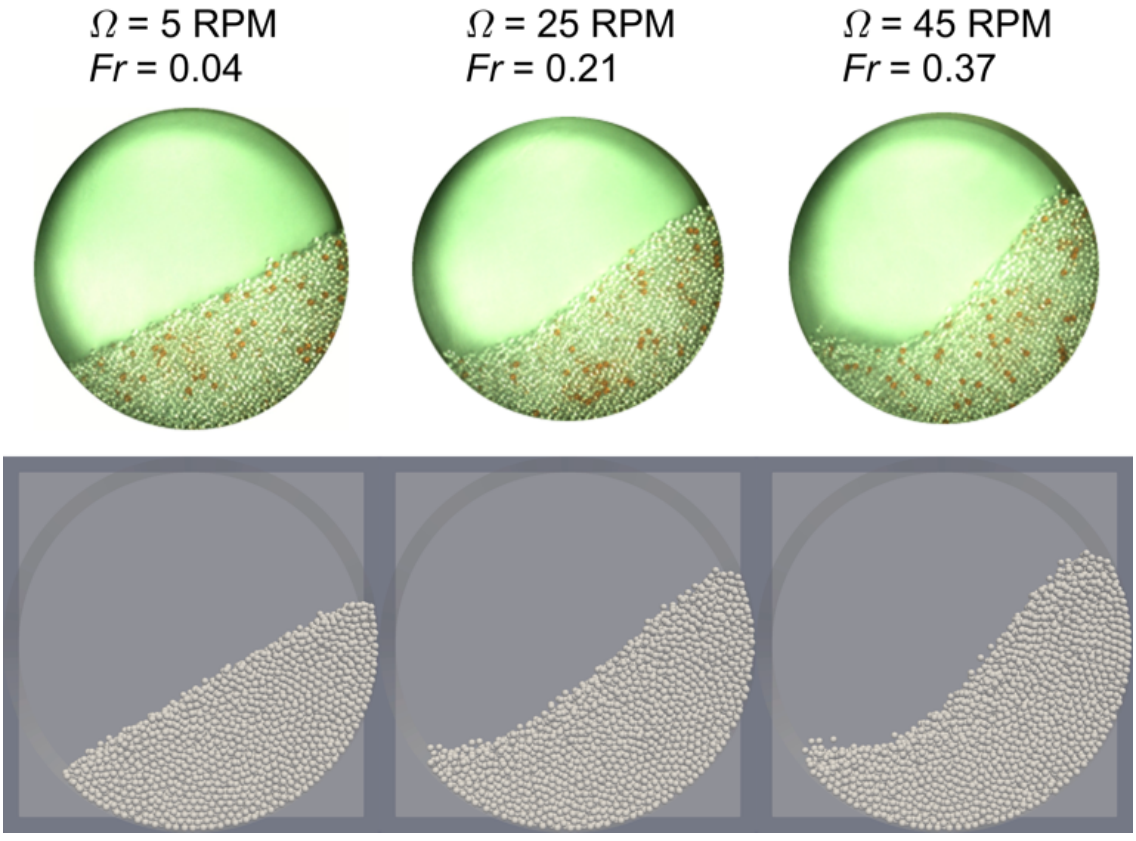

Figure 9: Snapshots comparing the experimental results (top row) with the simulations (bottom row) for the dry case. The left column correspond to rotation speed $\Omega = 5$ RPM, the middle column to $\Omega = 25$ RPM and the right column to $\Omega = 45$ RPM.

In order to make a quantitative comparison between the simulations and experiments, the angle of repose is calculated for each time step of each simulation. This is the angle between the surface of the bed and a horizontal line. Figure 10 shows the angle of repose as a function of time for varying rotations speeds. The drum starts rotating, and the angle of repose increases progressively. At a high enough slope angle, the first avalanche occurs, decreasing the angle of the slope rapidly, before stabilising quickly around an average value.

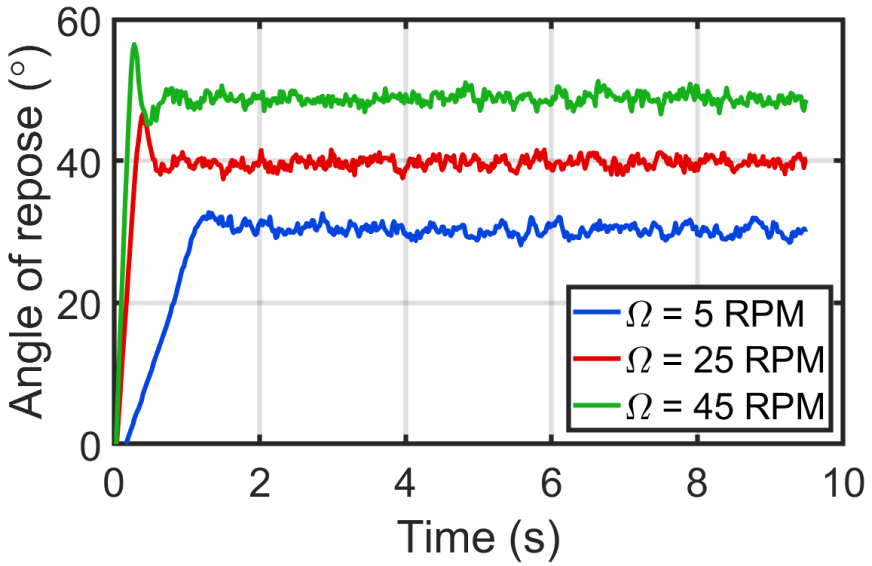

Figure 10: Angle of repose as a function of time for dry case. The blue line corresponds to rotation speed $\Omega = 5$ RPM, the red line to $\Omega = 25$ RPM and the green line to $\Omega = 45$ RPM.

The mean angle of repose is calculated by taking the average of the angle of repose for the last 6 seconds. The first few seconds are not included in the average, because the simulations takes a few seconds to reach an equilibrium state. Figure 11 shows the mean angle of repose as a function of rotation speed for both the experiments and the simulations. The error bars represent the standard deviation in the angle of repose. Experiments and simulations are both represented by separate measurements for each rotation speed and a linear fit through the varying rotation speeds. For low rotation speeds, 5RPM, the measured angle of the simulations is about 5 degrees higher than for the experiments, while for high rotation speeds, 45 RPM, the angle of the simulations is about 5° lower than the experiments.

The difference between experiments and simulations is relatively small. They also show a good agreement for a rotation speed $\Omega = 25$ RPM, which is the rotation speed that will be used in the experiments where liquid was added. Nevertheless, the sliding friction coefficient between particle and wall has been varied to test if this might give better agreement between simulation and experiment. This friction coefficient is one of the few parameters that could

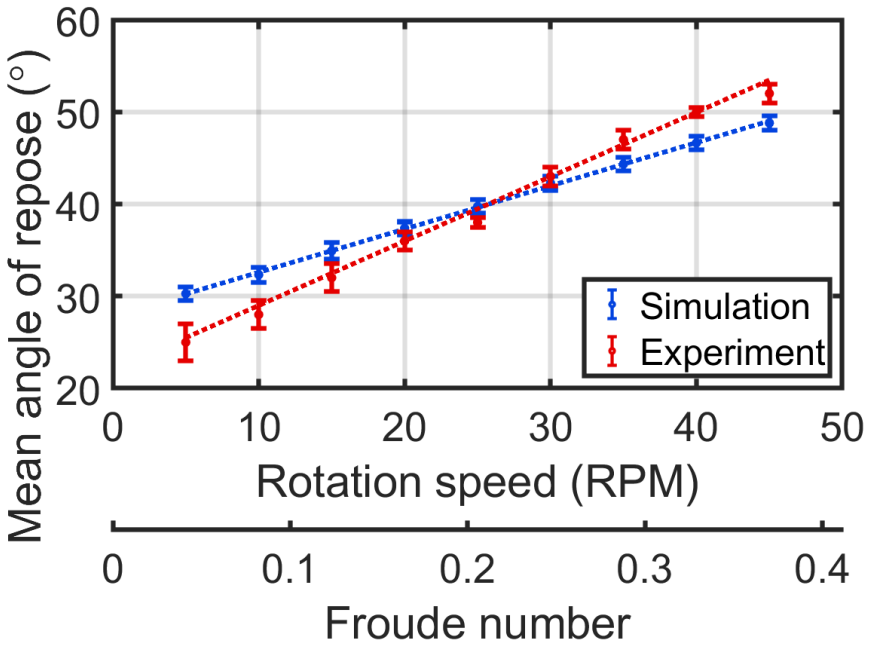

Figure 11: Angle of repose as a function of rotation speed for dry case. The blue line corresponds to the simulations and the red line to the experiments.

not be exactly measured for the experiments. Figure 12 shows the results of these simulations, where only the linear fit through the data is shown. The particle-wall friction coefficient was initially set to 0.3, and has here been varied to 0.2, 0.4 and 0.8. The angle of repose increases for all rotation speeds when increasing the particle wall friction coefficient, but only by a small amount. By increasing this coefficient from 0.3 to 0.8, the angle of repose at 45 RPM increases only by about 3 degrees, and is still smaller than the experiments. The initial sliding friction coefficient of 0.3 is still the best when looking at 25 RPM.

For the purpose of this work, the agreement between simulation and experiment can be considered good enough. But if better agreement is needed for further research, the parameters that are most likely to differ between simulation and experiment and have an impact on the angle of repose are friction coefficient, coefficient of restitution and collision time between particles and between particle and wall.

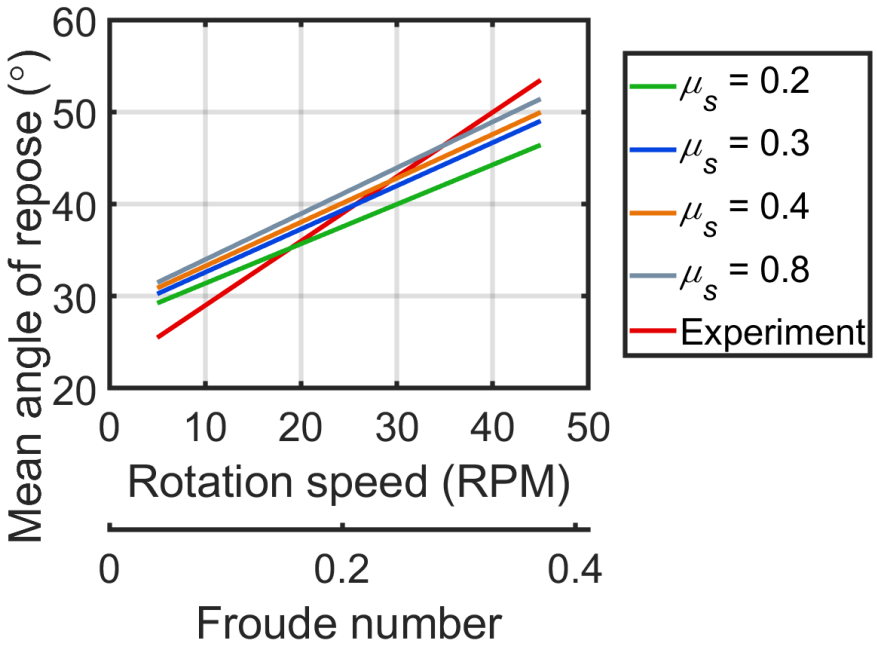

Figure 12: Angle of repose as a function of rotation speed for dry case, with varying sliding friction coefficient between a particle and the wall.

Figure 13 shows the flow speed for the simulations with rotation speed 5, 25 and 45 RPM. For the low rotation speeds, the flowing layer, where the particles are flowing down, is narrow and has a low velocity. For higher rotation speeds, the flowing layer get wider and the particles have higher velocities.

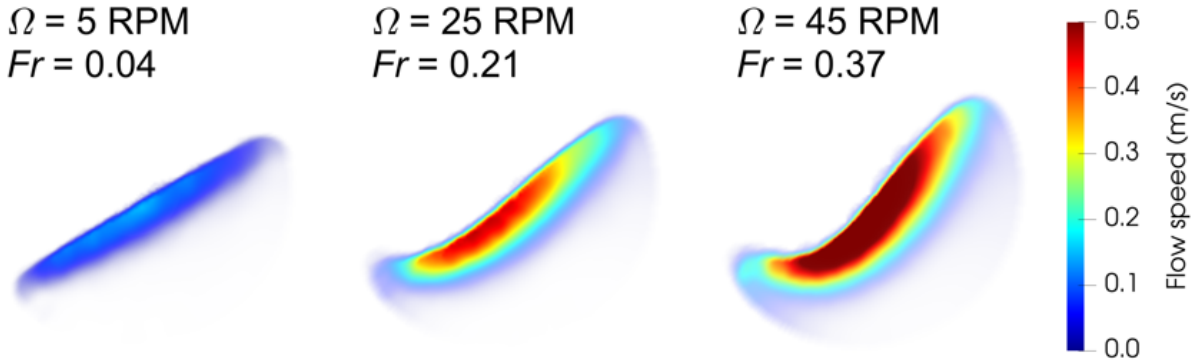

Figure 13: Flow speed of dry particles for varying rotation speeds.

From the flow speed, the granular temperature can be calculated, which is a measure for relative motion between particles. Figure 14 shows that for low rotation speeds, the particles in the flowing layer are flowing together, having a low granular temperature. For higher rotation speeds, the granular temperature becomes higher and is nonzero for a wider area. This again means that the flowing layer gets wider, and the particles in the flowing layer are no longer moving down together, but are bouncing off each other with more intensity.

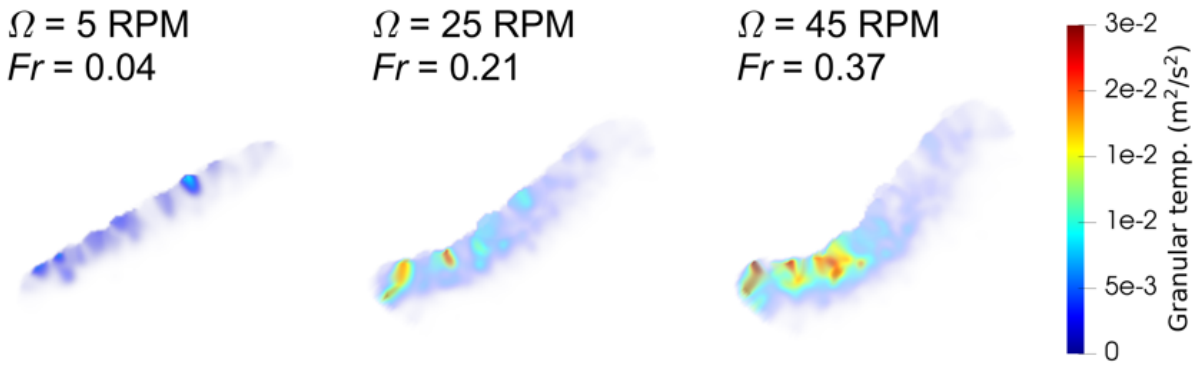

Figure 14: Granular temperature of dry particles for varying rotation speeds.

3.2 Wet case

3.2.1 Liquid distribution parameters

From the previous results, it can be concluded that the simulations meet the expectations and show good agreement with the experiments. The next step in this thesis is to include liquid in the simulation. In this step, it is assumed that the parameters that were already set, do not change when adding liquid. This means that the particle and wall properties remain unchanged, as well as the time step of the simulation. The liquid introduces a new adhesive force to the particles.

As explained in Section 2.4, no capillary bridges are formed between the particles and the front and back wall of the drum. The cylindrical wall does form bridges with particles, but these bridges make particles stick to the wall all the way around, making the calculation of the angle of repose difficult. These bridges are expected to have a smaller capillary force than the bridges between two particles, since the wall is made of wood. This effect will be investigated later in this thesis, but first these bridges will be turned off completely. With these bridges turned off, there are two parameters left to be determined before the different capillary forces can be simulated and compared with the experiments. The maximum bridge volume as characterized by β and the coefficient of distribution C_D, which determines the distribution of liquid after a bridge rupture. Simulations were performed with $F_c = 0.137$ mN, which corresponds to case 4 of the experiments performed by Jarray et al [12]. At this capillary force, $Bo = 0.73$, where Bo is the Bond number

$$Bo = \frac{3\gamma \cos\theta}{2r_p^2 \rho_p g}, \tag{14}$$

which represents the ratio of the capillary force to the gravitational force.

Wet simulations were performed at various C_D (0, 0.5 and 1), and different β ranging from 0.03 to 2, Table 2 shows the values of β that were used with their corresponding volume. The first indicator of the effect of these parameters on the behaviour of the system is the angle of repose. The mean angle of repose of these simulations is shown in Figure 15. For $C_D = 0$ and $C_D = 0.5$, the angle of repose does not change with varying β, while for $C_D = 1$, it decreases by a few degrees when increasing β. This decrease is less than two degrees, while the error bar is almost one degree, indicating a negligible decrease.

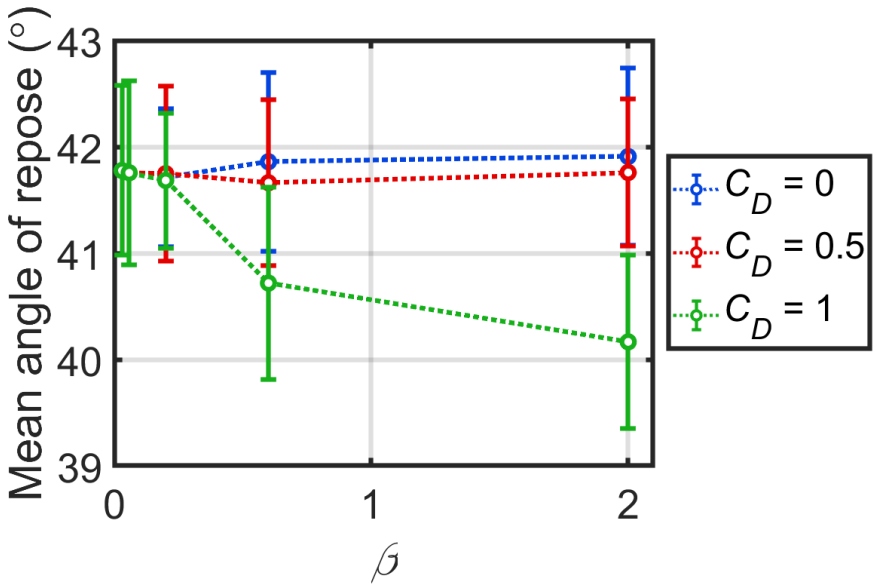

Figure 15: Angle of repose as a function of β. Different lines are for different values of C_D.

β	$V_{max}(nl)$
0.03	59
0.058	113
0.2	390
0.6	1172
2	3906

Table 2: Maximum bridge volumes in nanoliters corresponding to the different values of β.

We explore next the effect of β and C_D on the distribution of liquid in the capillary bridges. In order to do this, a probability density function (PDF) is calculated for the volume of liquid in a bridge. This is done by taking all the volumes of capillary bridges for a few time steps and counting how many bridges have a volume within each range of volumes. The value of the PDF corresponds to the probability density that capillary bridge has a certain volume. Taking the integral of the PDF in a range, gives the probability that the volume of a capillary bridge lies inside this range.

Initially, each particle has the same amount of liquid in a liquid film, with a volume of $V_{initial} = 654$ nl. Table 2 shows the values of β that were used in the simulations and their corresponding values of the maximum bridge volume.

Figure 16 shows the PDF of the capillary bridge volumes for $C_D = 0.5$ and varying values of β. Figure 16a shows this in a linear vertical scale, for bridge volumes smaller than 1000 nl, while Figure 16b shows this in a logarithmic vertical scale, for bridge volumes up to 4000 nl.

For the smallest two values of β, 0.03 and 0.058, the PDF shows a single peak at the bridge volume corresponding with the value of β. This means that all the non-empty bridges are saturated and $V = V_{max}$. This is expected, because the initial volume on each particle is almost 6 times larger then the maximum bridge volume suggested by Roy et al [26], corresponding to $\beta = 0.058$. A particle can form 5 bridges with other particles that contain the maximum bridge volume, and only the 6th bridge would not contain the maximum bridge volume. For $\beta = 0.2$, this occurs upon the formation of a second bridge on a particle. In this case, it will happen quite often that bridges are formed with less liquid than the maximum allowed volume. This also results in varying amounts of liquid being present on each particle, as the bridges that rupture do not all have the same volume. The same argument holds for higher values of β. For $\beta \geq 0.2$, the distribution curves have approximately the same shape, except for a peak at the maximum bridge volume. The height of this peak corresponds to the probability that a non-empty bridge has the maximum allowed volume. This peak becomes smaller for increasing values of β, because the limit is less strict. In Figure 16b, the curves show a linear decreasing trend, which corresponds to an exponential decay in the PDF.

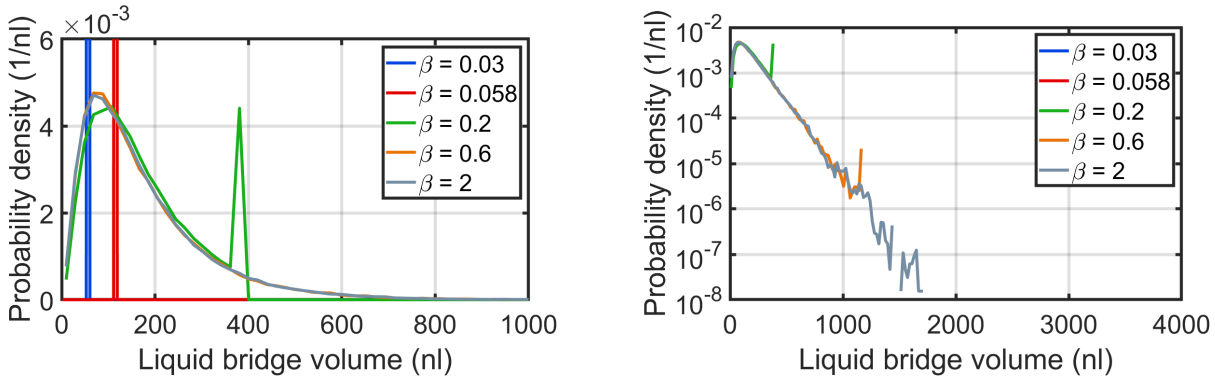

Figure 16: Probability density function of the capillary bridge volumes for $C_D = 0.5$ and varying values of β with (a), a linear vertical axis and (b), a logarithmic vertical axis.

Since the rupture distance increases with increasing β, so does the maximum interaction distance between particles. This means that the simulation takes longer for higher values of β. The current simulations take about 45 hours for $\beta = 0.6$ and about 65 hours for $\beta = 2$, which is a significant increase in simulation time. For simulations of this size, this is not really important, but for larger simulations, the value of β can have a very high impact on simulation time.

A compromise has to be found between a constraint on the bridge volume and the simulation time. From Figure 16b, it can be seen that the peak for β at $V = V_{max} = 1172$nl is several orders of magnitude smaller than the highest peak of this curve. This means that a relatively small number of bridges are actually limited by the constraint on the bridge volume. Therefore, $\beta = 0.6$ is the best value to use.

The same analysis can be performed for $C_D = 0$ and $C_D = 1$. Figure 17 shows the probability function of liquid bridge volumes for the simulations where the coefficient of distribution is equal to 0. This means that at each bride rupture, all the liquid is moved to the liquid films on the two particles, and none of the liquid is moved to already existing capillary bridges. In this case, the probability density function curves behave qualitatively the same. For the smallest two values of β, all bridges have the same volume and the probability density function consists of a single peak. For the largest two values of β, the curves are almost identical. The curve for $\beta = 0.2$ shows peaks with a half and a quarter of the maximum bridge volume, which are caused by the rupturing of the bridges. Since the liquid is distributed equally between the two particles and all the liquid is stored in the liquid films, bridge volumes are halved at every rupture. For $C_D = 0.5$, this does not occur, because the liquid is also distributed amongst the existing bridges.

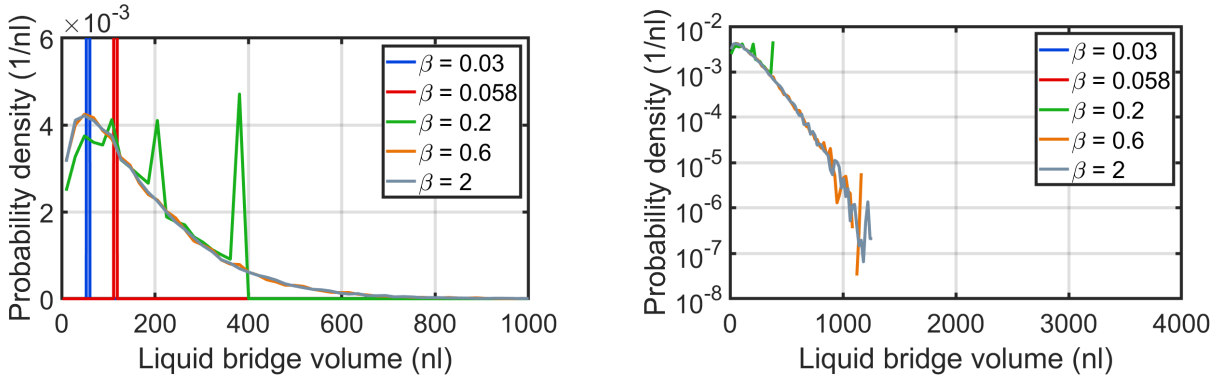

Figure 17: Probability density function of the capillary bridge volumes for $C_D = 0$ and varying values of β with (a), a linear vertical axis and (b), a logarithmic vertical axis.

From Figure 17, it can again be concluded that $\beta = 0.6$ is the optimal value to use. Between Figure 16 and Figure 17, there is no clear preference for either value of the coefficient of liquid distribution. But from a physical point of view, it makes more sense that the liquid moves around on the particle film and some of it flows into the existing capillary bridges. It is thus more reasonable to use $C_D = 0.5$.

Figure 18 shows the PDF of the liquid bridge volumes for $C_D = 1$. For simulations where the maximum bridge volume was limited, $\beta \leq 0.2$, the effect is small, since the existing bridges can't grow further. For higher values of β, the number of bridges is about 4 times smaller then for $C_D = 0.5$, and the probability density function is spread out to much higher volumes. This is not a good distribution, because the curve does not approach a stable value for higher values of β.

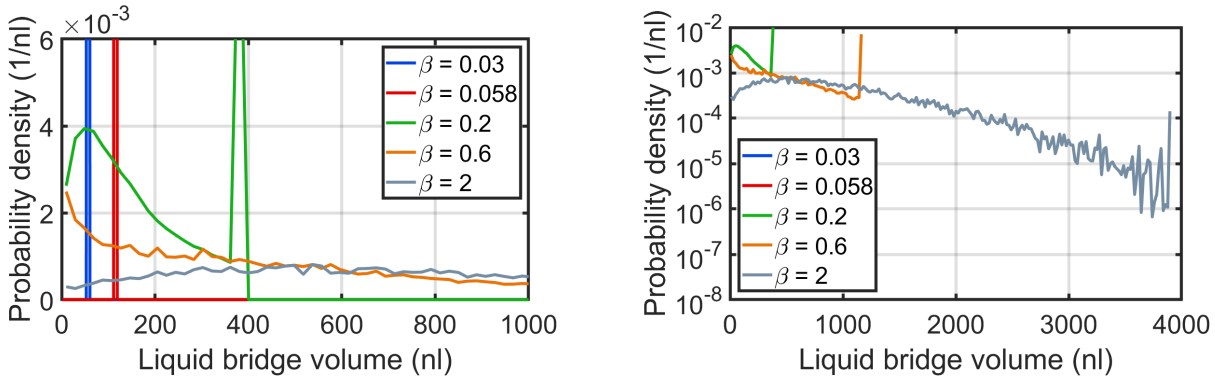

Figure 18: Probability density function of the capillary bridge volumes for $C_D = 1$ and varying values of β with (a), a linear vertical axis and (b), a logarithmic vertical axis.

A physical meaning behind C_D can be found in the ratio between the flow rate of liquid over the surface of a particle and the time between new contacts. If the liquid moves really slow over the surface of the particle, or the rate of new contacts is very high, then the liquid will not have had enough time to move into the existing bridges before forming a new bridge. This means that C_D is low, since most of the liquid will be available to form a new bridge and only some will have had time to move into an existing bridge. On the other hand, if the liquid moves fast over the surface of the particle, or the time between new contact formations is long, the liquid will have reached a new equilibrium between the bridges and liquid film, before a new bridge is formed. This means that C_D is high, since most of the liquid will have moved into the existing bridges before a new bridge is formed. Since there should be some liquid in each particles liquid film, $C_D = 1$ is not a realistic value, and it is more reasonable to use $C_D = 0.5$.

3.2.2 Alteration to the rupture code

At this point, the alteration to MercuryDPM, see Section 2.3, was implemented and tested for the same values of C_D and β. This alteration to the code is expected to have the biggest impact on the simulations with $C_D = 1$, since particles will almost never have liquid available to form new bridges. Meaning that a lot of new bridges will be formed. For lower values of C_D, the improvement will have much less impact. This is because each bridge rupture will leave some amount of liquid in the liquid films, so when particles make new contact it is much more likely that they have liquid available to form a new bridge.

Figure 19 again shows the mean angle of repose as a function of β, for varying values of C_D. The dashed lines show the results discussed before, while the solid lines show the results using the altered code. As can be seen, the alteration of the code has negligible impact on the mean angle of repose.

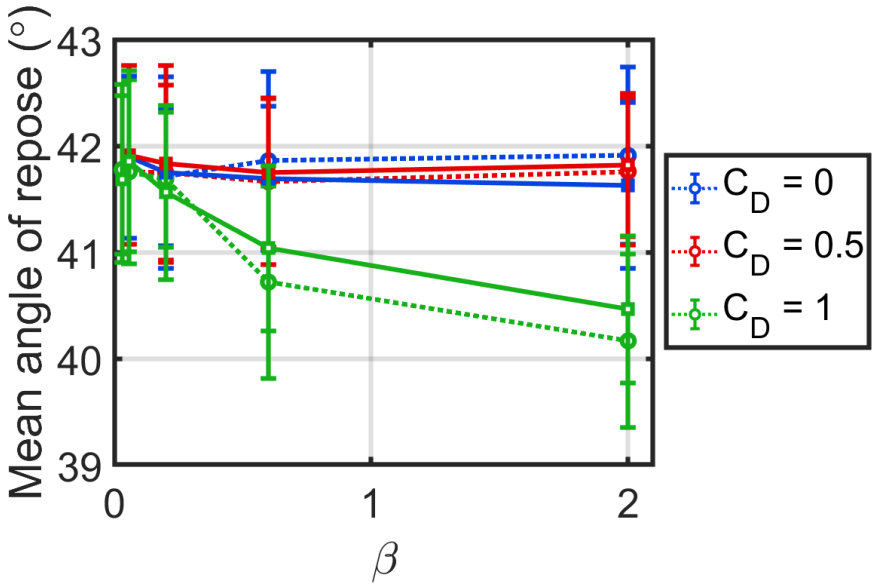

Figure 19: Angle of repose for varying β and C_D. Dashed lines correspond to the original liquid distribution code, the solid lines correspond to the altered code.

Figure 20 shows the PDF of the capillary bridge volumes for the different values of C_D and β. For $C_D = 0$ and $C_D = 0.5$, the alteration in the rupture code makes no significant difference in the PDF, which was expected. For $C_D = 1$ there are fewer bridges with extremely high volumes. This difference is the biggest for the highest value of β, since in this simulation, the bridge formation is restricted the least. This means that after almost each bridge formation, all the available liquid in the particle film is used to form the new bridge. Particle films are more often empty for $\beta = 2$ than for lower values of β, but even for this simulation, the improvement is still small. So all of this means that the altered code has a small positive

effect on some simulations, but no significant effect on most of the simulations. The value $C_D = 1$ still gives undesired results, confirming that $C_D = 1$ is not a realistic value to use. Since the altered code did not affect the simulations in a negative way, and does make more physical sense than the original liquid distribution code, it will be used throughout the rest of the simulations, in combination with $C_D = 0.5$ and $\beta = 0.6$.

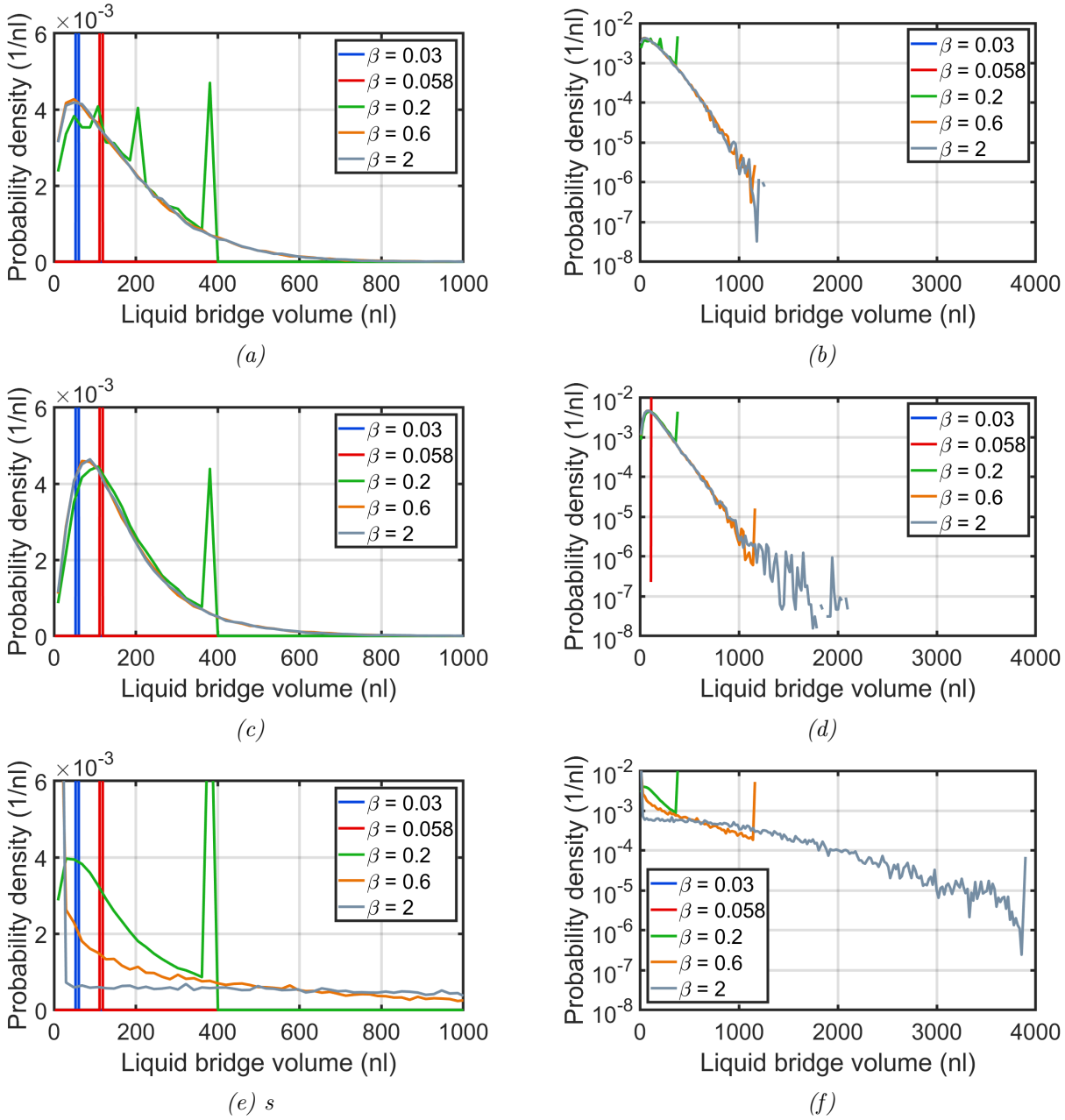

Figure 20: Probability density function of the capillary bridge volumes for the altered code. $C_D = 0$ with (a) a linear vertical axis and (b) a logarithmic vertical axis. $C_D = 0.5$ with (c) a linear vertical axis and (d) a logarithmic vertical axis. $C_D = 1$ with (e) a linear vertical axis and (f) a logarithmic vertical axis.

As mentioned before, there were no capillary bridges formed between particles and the drum up to this point. Now that the best values of C_D and β are determined, these bridges are introduced to the simulations. Because the front and back wall of the drum were coated in the experiment, bridges formation in the simulation were also switched off. But since the cylindrical wall of the drum was made of wood, bridges will form there, but not with the same capillary force as bridges that are formed between particles. This is because the contact angle of the liquid on the wood is different, and the wood is rougher than the particles, resulting in different behaviour of the capillary bridges.

To reflect this in the simulation, the contact angle of the capillary bridges between particle and wall have been varied following αF_C, where F_C is the capillary force for bridges between particles and α a fraction between 0 and 1. For $\alpha > 0.5$, the particles stick to the wall, which makes the calculations of the angle of repose impossible with the current method. Figure 21 shows the angle of repose as a function $\alpha \leq 0.5$. The red point refer to a simulation where no bridges are formed between particle and wall and the blue points to simulations where bridges are formed. It can be seen that the angle of repose is not influenced at all by the capillary bridges between particle and wall. For the rest of this thesis, $\alpha = 0.25$ has been chosen.

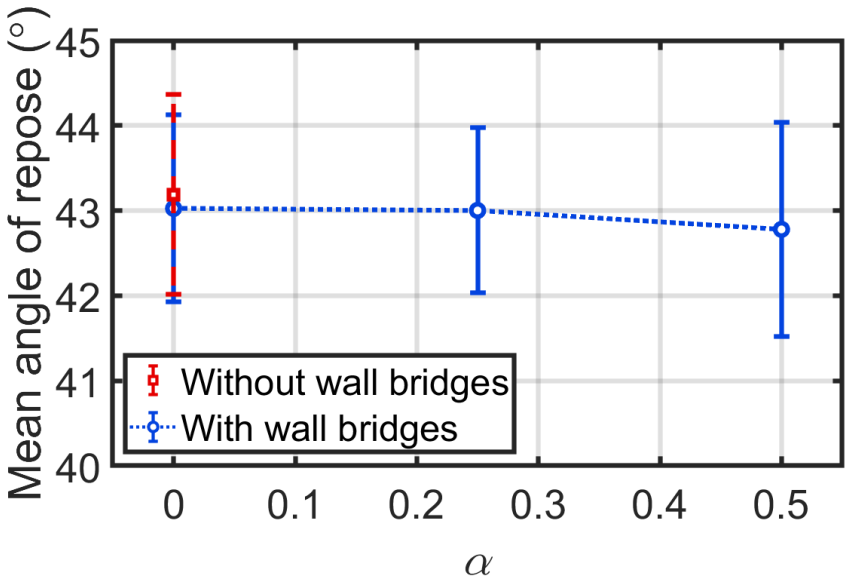

Figure 21: Mean angle of repose for varying capillary force for bridges between particles and wall.

3.2.3 Varying capillary force

Now that the simulation parameters are determined, the simulations representing the experiments can be performed. The surface tension and contact angle are chosen to represent the experiments, as shown in Table 3. Figure 22 shows the mean angle of repose as a function of the capillary force in mN. The red line represents the results from the experiments, the blue line those of the simulations. For low capillary forces, agreement is observed between experiments and simulations. For higher capillary forces, however, the mean angle of repose of the experiments is higher than that of the simulations. For the highest capillary force used, the difference is about 6°.

Case	γ (mN)	θ_c (°)	F_c	Bo	Ca
Case 2	72.0	90	0	0	-
Case 3	47.6	83	0.052	0.276	0.153
Case 4	38.0	61.5	0.137	0.732	0.049
Case 5	38.0	40.5	0.225	1.197	0.031
Case 6	47.6	47.5	0.253	1.350	0.028
Case 7	72.0	51.5	0.340	1.813	0.020

Table 3: An overview of the parameters for the wet case simulations used in this thesis.

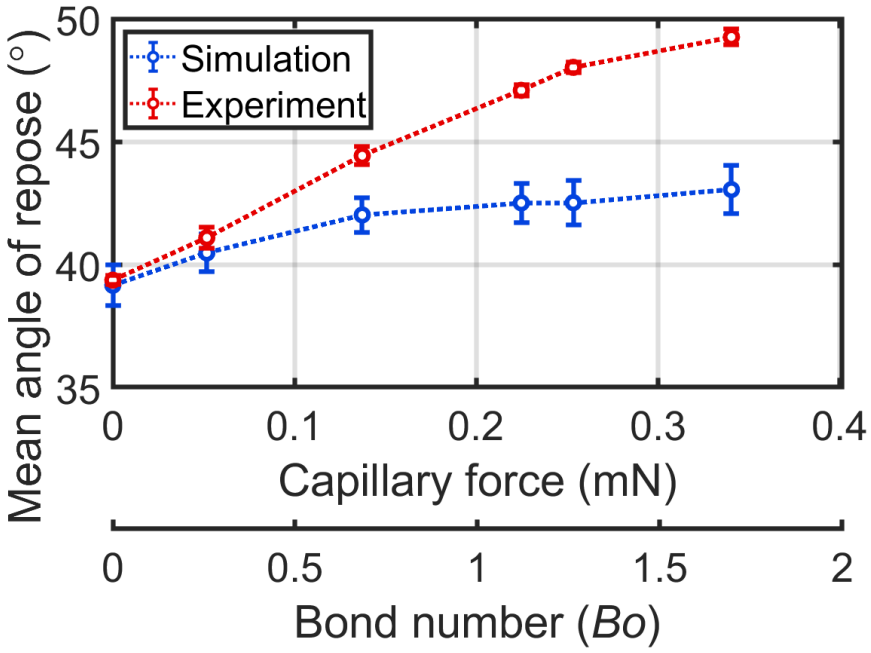

Figure 22: Angle of repose a function of the capillary force. Blue line are the simulations, red line the experiments.

A possible cause for this discrepancy, is that the capillary bridges exert more force in the experiments than is modelled in the simulations. This could be a result of inconsistencies in the experimental setup, or of a shortcoming in the capillary bridge model. To investigate this possibility, three more simulations have been performed with higher capillary forces. The resulting mean angles of repose for these simulations are shown in Figure 23. The angle of repose does increase with increasing capillary force, but still remains lower than for the experiments. The standard deviation of the angle of repose also increases significantly with increasing capillary force. This is because the capillary bridges hold the particles together with such high forces, that the system is no longer forming a continuous avalanche, but instead the particles are sticking together and behaving as a clump. This suggests that the system transitions to a new regime before the angle of repose is increased to values as high as the experiments. The origin of this discrepancy is still unknown, which prevents accurate DEM simulation.

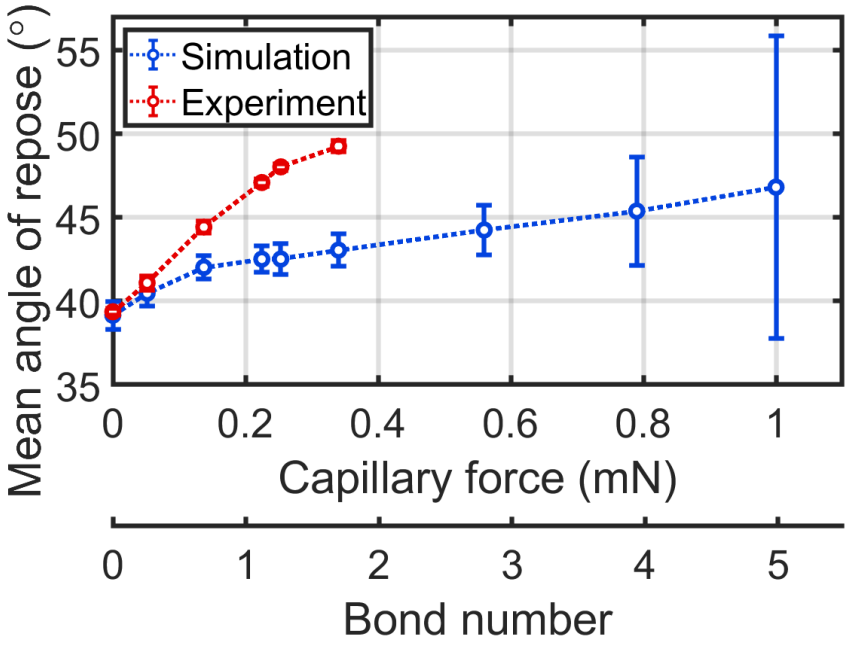

Figure 23: Angle of repose a function of the capillary force. Blue line are the simulations, red line the experiments.

Another possible cause of the difference between experiment and simulation is the viscosity of the liquid. In the simulations, the capillary bridges only exert capillary forces on the particles, while the viscous forces are neglected. To justify this simplification, Table 3 shows the capillary number

$$Ca = \frac{v_r \mu}{\gamma cos\theta} \tag{15}$$

where v_r is the relative velocity between particles, which is never larger than 2 m/s and μ is the dynamic viscosity. For each of the simulations, the capillarity number is smaller than 1, showing that the capillary forces are more important than the viscous forces.

From these result, no clear cause can be found for the discrepancy between simulation and experiment. A possible cause is the assumption that particle properties do not change between the different cases. Between the dry and wet case there might already be a large difference in the friction coefficients because the liquid lubricates the glass particles. Even between the different wet cases, the fraction of ethanol was varied and the particle surface properties were modified using a silanization process. It might be interesting to investigate the effect of the liquid composition and the silanization process on the friction coefficient of the particles. This in turn will have a significant impact on the angle of repose, as was already shown for the dry case in Figure 12.

To investigate the results of the simulations further the flow speed of the particles is calculated. Figure 24 shows the flow speed of the simulations in the top row and of the experiments in the bottom row. The left column corresponds to case 2, the middle row to case 5 and the right row to case 7 in Table 3. Visually, there is good agreement between simulation and experiment. For low capillary forces, there is a thin fast flow layer on top of the bed. For increasing capillary forces, this flowing layer gets slower and thicker, because particles stick together. By sticking together, the fastest moving particles get slowed down, while the particles below the fastest flowing layer get pulled along. This results in a thicker flower layer with a slower flow speed.

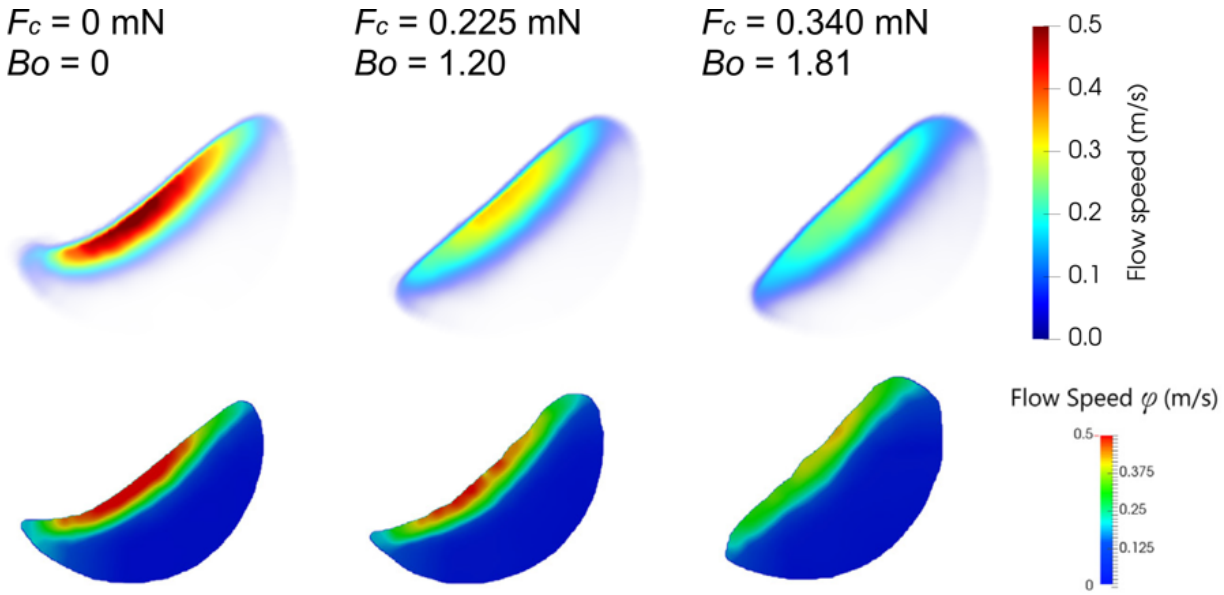

Figure 24: Flow speed of the simulations (top row) and experiments (bottom row).

From the flow speed, the granular temperature is calculated and compared to the experiments. Figure 25 shows the granular temperature of the simulations in the top row and of the experiments in the bottom row. The left column corresponds to case 2, the middle row to case 5 and the right row to case 7. Again there is a good qualitative agreement between simulation and experiment, although the values are a few orders of magnitude different from each other. This difference is most likely due to the fact that the experiments were analysed using a PIV-method. This means that the velocity of the separate particles was not measured, but rather the velocity in a certain grid cell. This has a large impact on the actual values of the granular temperature, meaning that a quantitative comparison is not possible. Qualitatively both experiments and simulations show that for low capillary forces, the particles bounce around at the bottom, resulting in high granular temperature there. For increasing capillary forces, this effect disappears, again because the particles in the flowing layer stick together more, resulting in a more uniform flow and thus lower granular temperature. It can also be seen from the granular temperature that the flowing layer get thicker for larger capillary forces.

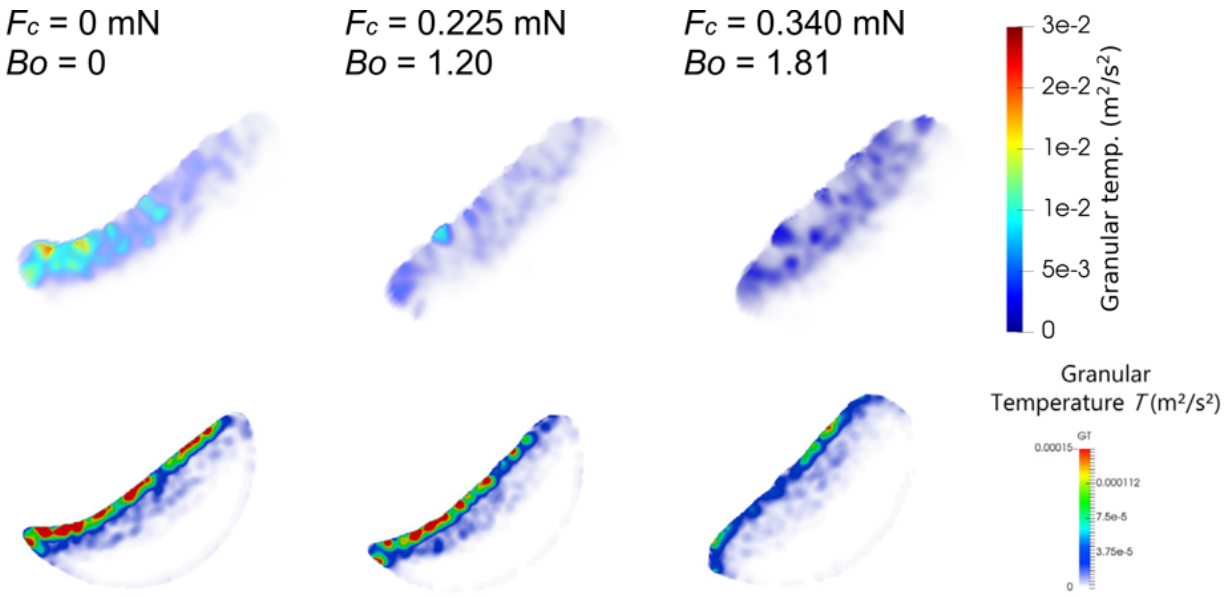

Figure 25: Granular temperature of the simulations (top row) and experiments (bottom row).

The final property of the system that has been visualized is the liquid distribution, see Figure 26. For the lowest capillary force, the liquid moves toward the centre of the drum, while for the higher capillary forces this does not happen. From other research [15], it has been determined that the liquid moves away from regions where there are a lot of bridge ruptures, which is linked to regions of high strain rate. Intuitively, it can be seen that for the lowest capillary force, there are a lot of bridge ruptures at the bottom of the bed, where

the particles bounce around. Due to these bridge ruptures, the liquid moves away from this region. Due to the rotating of the drum, a ring with less liquid forms around the centre where all the liquid is concentrated. For higher capillary forces, the particles don't bounce around in this region anymore, which translates into fewer bridge ruptures. The region of highest bridge rupture rate will now be more to the centre of the drum, resulting in a slow transport of liquid outside of the core of the particles bed. This can be seen to a small extent in the liquid distribution for the highest capillary force simulation. The centre has a little lower concentration of liquid than the outer zone of the bed.

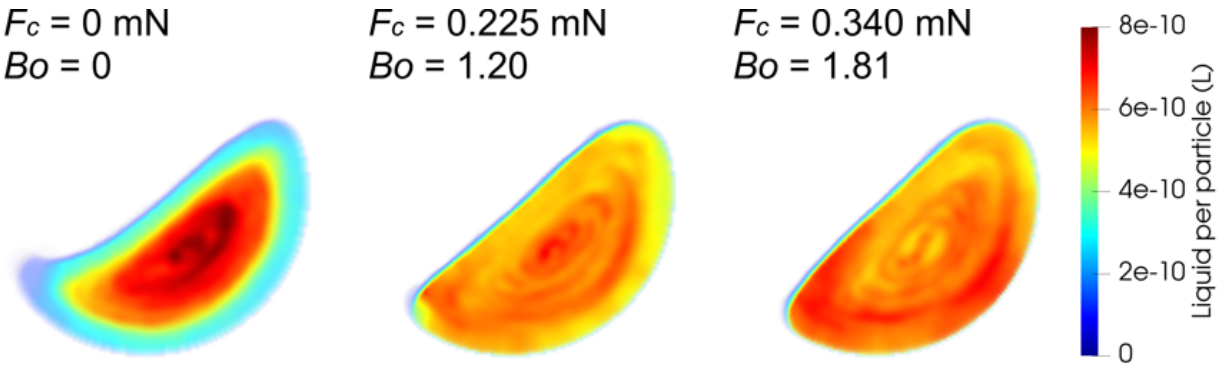

Figure 26: Liquid distribution of the simulations for various capillary forces.

To find out if the liquid is indeed slowly moving away from the centre, the simulation with the highest capillary force has been allowed to run for 10 times as long as the other simulations. The resulting liquid distribution after this longer simulation is shown in Figure 27. The result is as expected, where the liquid has moved away from the centre even more clearly, although the centre is not as dry as the outer ring is in the simulation with the lowest capillary force.

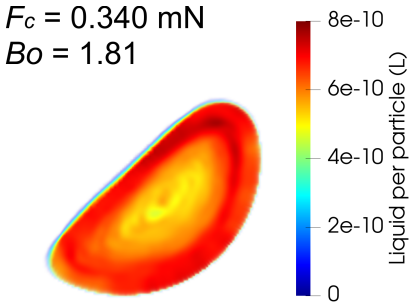

Figure 27: Liquid distribution for case 7 for a 10 times longer simulation time.

In the experiments, the liquid distribution was only visualized for a single experiment with low capillary force, although it is not clear which value exactly. In this experiment, the same behaviour was seen as our simulation with the lowest capillary force, namely the

liquid congregating in the centre of the drum, see Figure 28. It would be interesting to perform experimental measurements for high capillary force cases, in order to validate our DEM simulations.

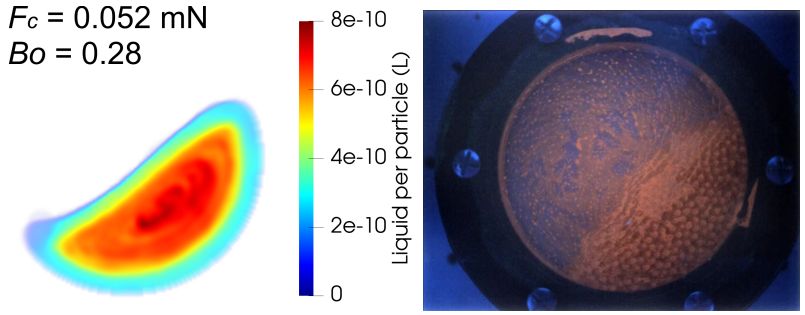

Figure 28: Liquid distribution for (a) case 3 of the simulation and (b) an experiment with low capillary force.

Because the liquid is concentrating in different regions of the bed for different capillary forces. The concentration of the liquid means that the system might not be in the pendular state anymore, while the capillary bridge model does assume this. This assumption might explain the difference in angle of repose between simulation and experiment. The best way to test this would be to perform the experiments again with less liquid. This would ensure that the experiments are in the pendular state in every part of the bed.

Figure 29 shows the strain rate of the simulations for various capillary forces. For the lowest capillary force, the highest strain rate is at the bottom of the flowing layer, while for higher capillary forces, the strain rate decreases. The region of high strain rate also moves away from the flowing layer, toward the centre of the bed. This suggests that the liquid does move away from the region of highest strain rate, resulting in the behaviour shown in Figure 26.

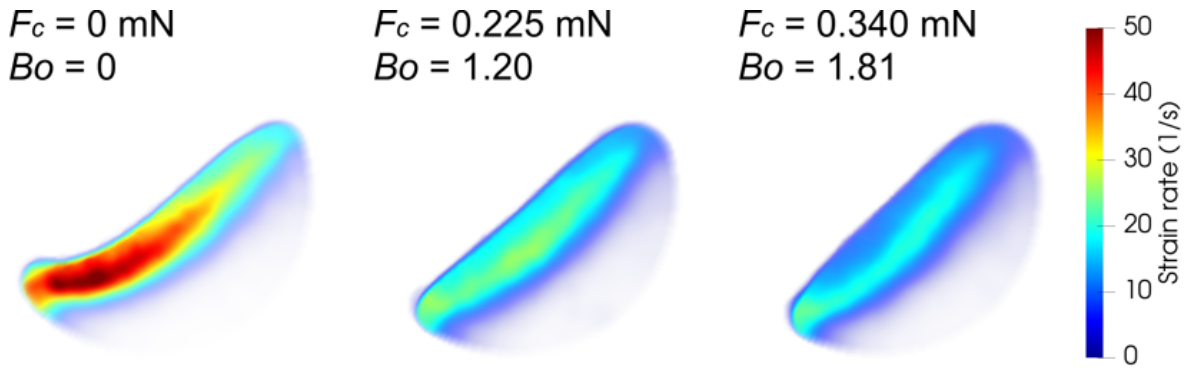

Figure 29: Strain rate of the simulations for various capillary forces.

4 Conclusion

In this work, simulations of dry and wet granular material in a rotating drum were compared with experiments. For the dry case, a good agreement of the angle of repose was found between simulation and experiment for varying rotation speeds. The best agreement was found at $\Omega = 25$ RPM. The flow speed and granular temperature increase for high rotation speeds, while flowing layer becomes wider and faster.

Wet case simulations were performed at a rotation speed $\Omega = 25$ RPM. The impact of the coefficient of distribution and maximum bridge volume on the flow was investigated, along with an improvement in the liquid distribution code of MercuryDPM. The effect of capillary force on the flow was investigated by varying the contact angle and surface tension of the liquid. A difference of 6° between simulation and experiment was found for the contact angle of the highest capillary force. The cause of this difference was not found in this work, but it is suggested that the friction coefficient of the particles might vary between the different experiments, while it was kept constant in the simulations. The flow speed and granular temperature, on the other hand, agree well with the experiments.

Finally, it has been shown that the liquid migrates to the center of the bed for low capillary forces, while it migrates away from the center for higher capillary forces. It is observed that the liquid migrates away from the location with the highest strain rate, which corresponds to the region where the most bridges rupture.

The results reported in this work open several prospects. For instance, the distribution of the liquid shows that the migration depends on the capillary force. This could be investigated further using experiments. Further more, the simulation and analysis methods used here should be applied to and checked against other granular flow simulations (e.g. silo, inclined plane, chute flow, etc.).

References

[1] E. Bruce Pitman and C. Camil Nichita. Computing granular avalanches and landslides. *Physics of Fluids 15: 3638*, 2003.

[2] Juan G. Osorio and Fernando J. Muzzio. Effects of processing parameters and blade patterns on continuous pharmaceutical powder mixing. *Chemical Engineering and Processing - Process Intensification 109*, pages 59–67, 2016.

[3] Allison Crouter and Lauren Briens. Methods to assess mixing of pharmaceutical powders. *AAPS PharmSciTech 20*, page 84, 2019.

[4] Patrick Cullen, Serafim Bakalis, and Carl Sullivan. Advances in control of food mixing operations. *Current opinion in food science*, pages 89–93, 2017.

[5] K.S.N. Vijay and Vishal Mishra. Flow behaviour of granular materials in pharmaceutical and food industry. *The Pharmstudent 28*, pages 12–17, 2017.

[6] Pierre Lambert, Alexandre Chau, and Alain Delchambre. Comparison between two capillary forces models. *Langmuir 24*, pages 3157–3163, 2008.

[7] P. Tegzes, T. Vicsek, and P. Schiffer. Development of correlations in the dynamics of wet granular avalanches. *Physical Review E 67: 051303*, 2003.

[8] C. Soria-Hoyo, J.M. Valverde, and A. Castellanos. Avalanches in moistened beds of glass beads. *Powder technology 196*, pages 257–262, 2009.

[9] Sarah Nowak, Azadeh Samadani, and Arshad Kudrolli. Maximum angle of stability of a wet granular pile. *Nature physics VOL 1*, 2005.

[10] Jean Rajchenbach. Flow in powders: From discrete avalanches to continuous regime. *Physical Review Letters 65:18*, 1990.

[11] R.Y. Yang, R.P. Zou, and A.B. Yu. Microdynamic analysis of particle flow in a horizontal rotating drum. *Powder Technology 130*, pages 138–146, 2003.

[12] Ahmed Jarray, Vanessa Magnanimo, and Stefan Luding. Wet granular flow control through liquid induced cohesion. *Powder Technology 341*, pages 126–139, 2018.

[13] Qing Xu, Ashish V. Orpe, and Arshad Kudrolli. Lubrication effects on the flow of wet granular materials. *Physical Review E 76*, page 031302, 2007.

[14] P.Y. Liu, R.Y. Yang, and A.B. Yu. Dynamics of wet particles in rotating drums: Effect of liquid surface tension. *Physics of Fluids 23*, page 013304, 2011.

[15] Roman Mani, Dirk Kadau, Dani Or, and Hans J. Herrmann. Fluid depletion in shear bands. *Physical Review Letters 109*, page 248001, 2018.

[16] Roman Mani, Dirk Kadau, and Hans J. Herrmann. Liquid migration in sheared unsaturated granular media. *Granular Matter 15*, pages 447–454, 2013.

[17] Steffen Schmelzle and Herrmann Nirschl. Dem simulations: mixing of dry and wet granular material with different contact angles. *Granular Matter 20*, pages 1–13, 2018.

[18] Bhageshvar Mohan, Christoph Kloss, Johannes Khinast, and Stefan Radl. Regimes of liquid transport through sheared beds of inertial smooth particles. *Powder Technology 264*, pages 377–395, 2014.

[19] Sudeshna Roy, Abhinendra Singh, Stefan Luding, and Thomas Weinhart. Micro-macro transition and simplified contact models for wet granular materials. *Comp. Part. Mech. 3*, pages 449–462, 2016.

[20] Cesare M. Cejas, Lqwrence A. Hough, Cristian Frétigny, and Rémi Dreyfus. Effect of geometry on the dewetting of granular chains by evaporation. *Soft Matter 14*, page 6994, 2018.

[21] T. Weinhart, L. Orefice, and M. Post et al. Fast, flexible particle simulations — an introduction to mercurydpm. *Computer Physics Communications*, 249:107129, 2020.

[22] Sudeshna Roy, Bert J. Scheper, Harmen Polman, Anthony R. Thornton, Deepak R. Tunuguntla, Stefan Luding, and Thomas Weinhart. Surface flow profiles for dry and wet granular materials by particle tracking velocimetry; the effect of wall roughness. *European Physical Journal E. 42:14*, 2018.

[23] Stefan Luding. Introduction to discrete element methods. *Discrete modelling of geomaterials*, pages 785–826, 2008.

[24] Stefan Luding. Collisions & contacts between two particles. *Physics of Dry Granular Media*, pages 285–304, 1998.

[25] Christopher D. Willet, Michael J. Adams, Simon A. Johnson, and Jonathan P. K. Seville. Capillary bridges between two spherical bodies. *Langmuir 16*, pages 9396–9405, 2000.

[26] Sudeshna Roy, Stefan Luding, and Thomas Weinhart. Liquid redistribution in sheared wet granular media. *Physical review E 98*, page 052906, 2018.

[27] M. Scheel, R. Seemann, M. Brinkmann, M. Di Michiel, A. Sheppard, B. Breidenbach, and S. Herminghaus. Morphological clues to wet granular pile stability. *Nature Materials 7*, pages 189–193, 2008.

[28] Eric W. Weisstein. *Circular Segment*, (accessed 19-11-2020). `https://mathworld.wolfram.com/CircularSegment.html`.

[29] Stefan Luding, Karsten Manetsberger, and Johannes Müllers. A discrete model for long time sintering. *Journal of the mechanics and physics of solids 53(2)*, pages 455–491, 2005.

[30] Nikolai V. Brilliantov, Frank Spahn, Jan-Martin Hertzsch, and Thorsten Pöschel. Model for collisions in granular gases. *Physical review E 53:5*, 1996.

[31] Ayachit and Utkarsh. The paraview guide: A parallel visualization application. *Kitware*, 2015.

Appendices

A Changes to MercuryDPM

In the process of this thesis, I have made some changes to the kernel of MercuryDPM. Since I started using MercuryDPM 2 years ago, the kernel itself has been updated in the meantime. In this chapter, I will explain which changes I made to the version that I downloaded 2 years ago, and I will make a note at the changes that no longer seem to be necessary in a newer version of MercuryDPM, which I downloaded on 06-11-2020.

Outputs

The code was edited in such a way to output the following parameters in the .vtu files:

- Liquid film volume. This is no longer needed in the newer version.
- Capillary bridge volume. This is no longer needed in the newer version.
- Capillary force of each capillary bridge.
- Number of capillary bridges connected to each particle.
- Number of 'empty capillary bridges' connected to each particle. These are contacts between particles where a capillary bridge would have formed, if there had been liquid available when the contact was made.

And the following changes were made to the existing outputs in the .vtu files:

- When two particles are not in contact, the contact radius was given as NaN, but this gives problems when using Paraview to analyse the .vtu files. So the contact radius was set to 0 when particles are not in contact. The same solution is already implemented in the newer version of MercuryDPM.
- Throughout the code, every parameter that is written to a .vtu file gets the type float32. But these parameters are actually stored as doubles. This means that in some cases, the value of the parameter is so small, that in float32 it would be stored as 0, while it is written as a nonzero value. This again gives problems in Paraview, it tries to read a float64 as a float32, which can give errors in certain situations. To solve this problem, all the functions getTypeVTK() return float64 instead of float32.

I have also added a single input parameter to the species, to prevent forming bridges. This parameters is simply a 1 or a 0, and is checked when the a bridge formation occurs. If the parameter is 0, the bridge is not formed. This was meant to make it easy to turn on and off

the bridge formation between particles and the different walls. I now realize that it would have been better to use a different species for these walls, that does not use capillary bridges at all.

Finally, the improvement in the rupture code that was discussed earlier in this report was implemented. This improvement is in searching for the existing capillary bridges. In the original code, a bridge is formed when two particles first come into contact with each other, unless there is no liquid available in the liquid films of both particles. At these contacts, no capillary bridge is formed, even when liquid does become available after a bridge rupture. The improvement is meant to include these 'empty capillary bridges' when distributing the liquid after a bridge rupture. This is accomplished by changing a single line that occurs once in the function GetNumberOfContacts() and four times in the function Rupture():

```
Replace:
if (j != this && jIParticle != nullptr && j->getLiquidBridgeVolume() != 0.0)
With:
if (j != this && jIParticle != nullptr && (j->getLiquidBridgeVolume() != 0.0
|| (j->getWasInContact()==true && j->getSpecies()->getFormBridges()==1)))
```

B Strain rate

The strain rate in this thesis has been calculated as explained in Section 2.7. These calculations are compared with the result of a more exact computation using the analysis tool tav12 written by Prof.dr. Stefan Luding. Figure 30 shows the strain rate for case 2, Figure 31 shows the strain rate for case 5 and Figure 32 shows the strain rate for case 7. In each of these figures, the top two images show the results from the analysis tool tav12, while the bottom image shows the results obtained using a python code and visualized using ParaView [31]. For all three cases, the general shape of the strain rate agrees well between the two methods. For increasing capillary force, the strain rate decreases and the peak moves down into the bed.

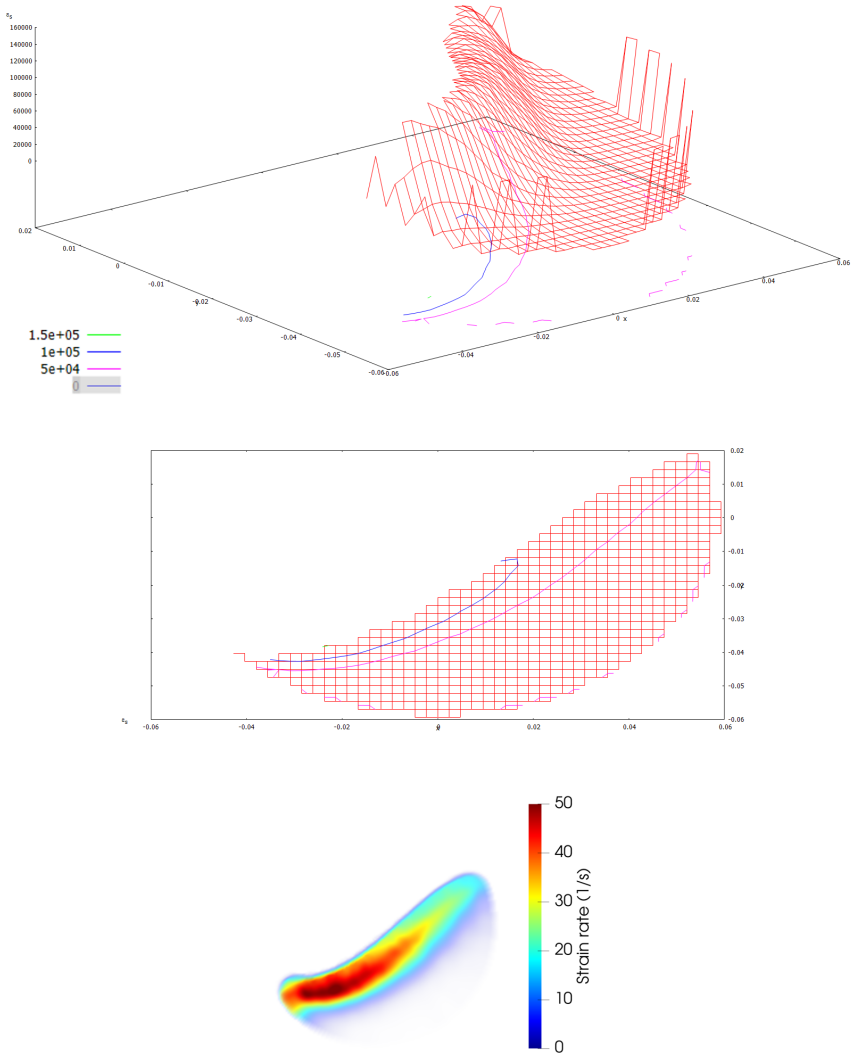

Figure 30: Strain rate case 2

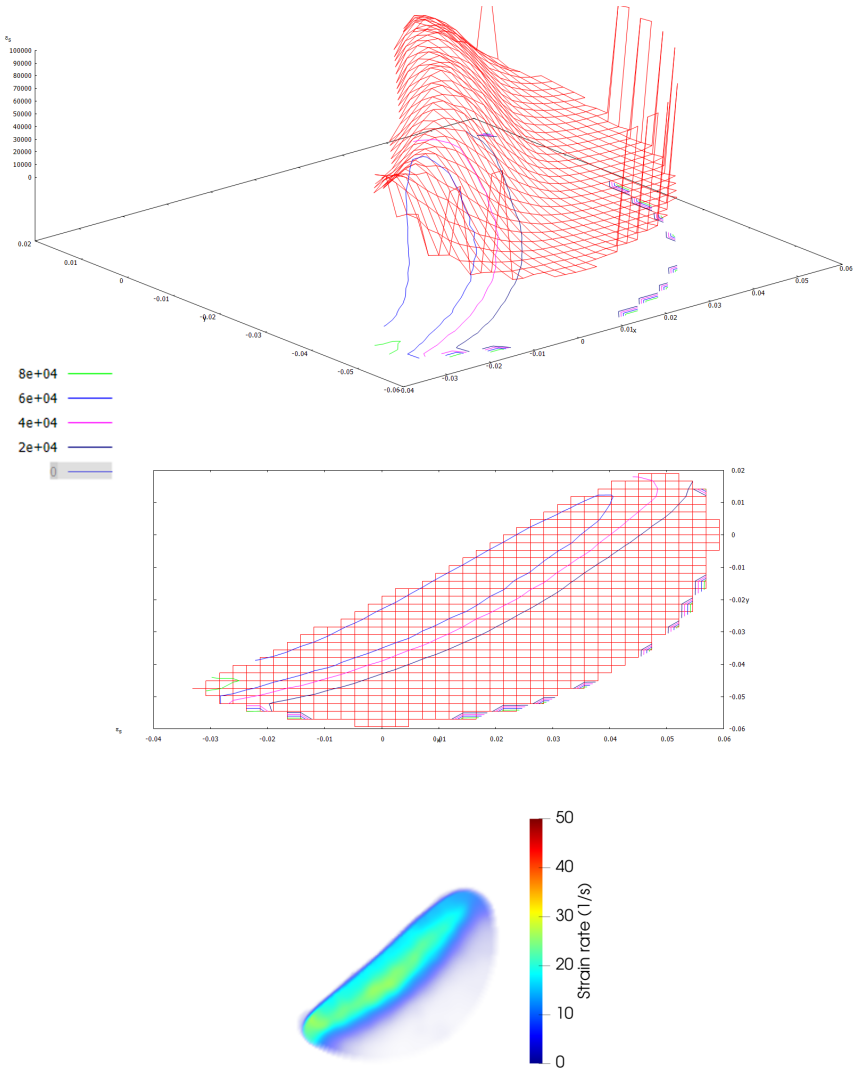

Figure 31: Strain rate case 5

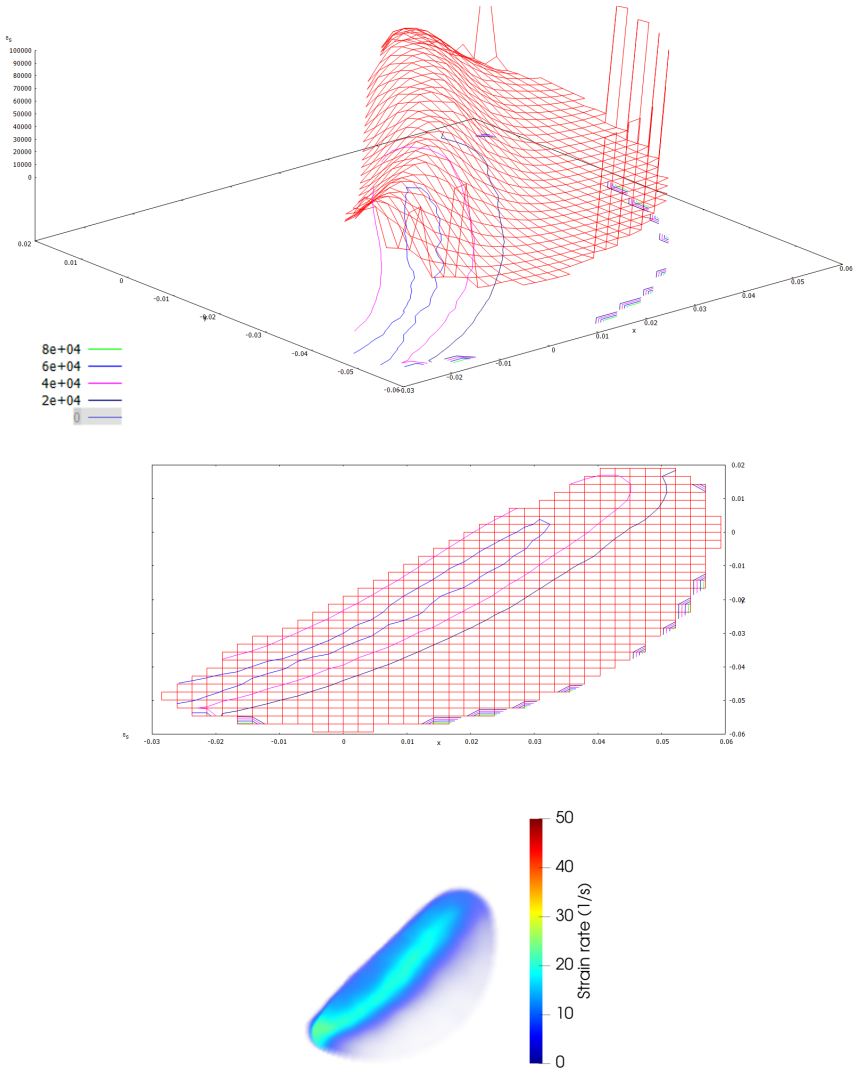

Figure 32: Strain rate case 7